

JGR Space Physics

RESEARCH ARTICLE

10.1029/2019JA026873

Special Section:

Equatorial Aeronomy: New results from the 15th International Symposium on Equatorial Aeronomy (ISEA-15) and beyond

Key Points:

- The midlatitude broad SED and SED plume are formed approximately 1–2 hr after a sudden enhancement of the high-latitude convection
- The major cause of the midlatitude broad SED is due to an upward motion of the ionosphere by the enhanced convection electric field
- The EIA intensification occurs in the evening sector approximately 1 hr after the prompt penetration of the electric field to the equator

Correspondence to:

A. Shinbori,
shinbori@isee.nagoya-u.ac.jp

Citation:

Shinbori, A., Otsuka, Y., Sori, T., Tsugawa, T., & Nishioka, M. (2020). Temporal and spatial variations of total electron content enhancements during a geomagnetic storm on 27 and 28 September 2017. *Journal of Geophysical Research: Space Physics*, 125, e2019JA026873. <https://doi.org/10.1029/2019JA026873>

Received 22 APR 2019

Accepted 28 APR 2020

Accepted article online 19 JUN 2020

Temporal and Spatial Variations of Total Electron Content Enhancements During a Geomagnetic Storm on 27 and 28 September 2017

Atsuki Shinbori¹ , Yuichi Otsuka¹ , Takuya Sori¹ , Takuya Tsugawa², and Michi Nishioka² 

¹Institute for Space-Earth Environmental Research, Nagoya University, Nagoya, Japan, ²National Institute of Information and Communications Technology, Koganei, Tokyo, Japan

Abstract Temporal and spatial evolutions of total electron content (TEC) and electron density in the ionosphere during a geomagnetic storm that occurred on 27 and 28 September 2017 have been investigated using global TEC data obtained from many Global Navigation Satellite System stations together with the ionosonde, geomagnetic field, Jicamarca incoherent scatter and Super Dual Auroral Radar Network (SuperDARN) radar data. Our analysis results show that a clear enhancement of the ratio of the TEC difference (rTEC) first occurs from noon to afternoon at high latitudes within 1 hr after a sudden increase and expansion of the high-latitude convection and prompt penetration of the electric field to the equator associated with the southward excursion of the interplanetary magnetic field. Approximately 1–2 hr after the onset of the $h_m F_2$ increase in the midlatitude and low-latitude regions associated with the high-latitude convection enhancement, the rTEC and $f_o F_2$ values begin to increase and the enhanced rTEC region expands to low latitudes within 1–2 hr. This signature suggests that the ionospheric plasmas in the F_2 region move at a higher altitude due to local electric field drift, where the recombination rate is smaller, and that the electron density increases due to additional production at the lower altitude in the sunlit region. Later, another rTEC enhancement related to the equatorial ionization anomaly appears in the equatorial region approximately 1 hr after the prompt penetration of the electric field to the equator and expands to higher latitudes within 3–4 hr.

1. Introduction

When solar wind disturbances with a strong southward interplanetary magnetic field (IMF) arrive at the Earth's magnetosphere, the magnetospheric convection is enhanced via the magnetic merging process between the southward IMF and northward geomagnetic field at the dayside magnetopause. Based on the enhanced magnetospheric convection, a ring current develops in the inner magnetosphere and causes a geomagnetic storm, which is characterized by a significant depression of the H component of the geomagnetic field in low- and middle-latitude regions. The geomagnetic storm severely changes the electromagnetic and plasma environments in the magnetosphere and ionosphere and the neutral composition of the thermosphere. At a height of the ionosphere, several prominent storm time ionospheric disturbances are observed over a wide region, that is, from high latitudes to the equator. These phenomena include a tongue of ionization (TOI) at the polar cap, storm-enhanced density (SED) at middle and low latitudes, and enhanced equatorial ionization anomaly (EIA) in the equatorial region. Because the spatial distribution of the electron density drastically changes because of these storm time ionospheric phenomena, electron density disturbances increase the satellite positioning error. Therefore, it is important to monitor the temporal and spatial evolutions of global ionospheric disturbances during the development and decay of geomagnetic storms.

Based on ionospheric observations obtained at the incoherent radar facility at Millstone Hill, an electron density enhancement with increasing F region peak height appears in the afternoon to evening sectors during the main phase of geomagnetic storms (e.g., Buonsanto, 1995a, 1995b, 1999; Evans, 1973; Mendillo et al., 1972; Papagiannis et al., 1971). This phenomenon is called “dusk effect.” Based on the long-term observation data obtained from Millstone Hill incoherent radar data, Buonsanto (1995b) proposed that the generation mechanism of the dusk effect results in the combination of the transport of high-density plasma from low to high latitudes, neutral wind, and neutral composition changes. Foster (1993) renamed the dusk

effect “SED,” which is defined as the increase in the electron density with an increasing F region peak height and latitudinal stream-like structure around the enhanced sunward convection region. Foster (1993) also showed that the SED phenomenon tends to appear equatorward in the midlatitude trough (e.g., Yang et al., 2015, 2016) and is caused by the equatorward expansion of the enhanced two-cell convection associated with the development of geomagnetic storms.

Based on the development of Global Positioning System (GPS) techniques and worldwide expansion of dense regional GPS receiver networks, the global change in the ionospheric electron density distribution during geomagnetic storms has been investigated using the world map of the GPS total electron content (TEC) in combination with ionospheric radars, ionosondes, optical imagers, and magnetometers (e.g., Balan et al., 2009, 2010; Coster et al., 2003, 2017; David et al., 2011; Foster et al., 2005; Heelis, 2017; Liu, Wang, Burns, Yue, et al., 2016; Liu, Wang, Burns, Solomon, et al., 2016; Maruyama, 2006; Maruyama et al., 2004, 2013; Sori et al., 2019; Thomas et al., 2013; Tsurutani et al., 2004; Yizengaw et al., 2006; Zhao et al., 2005; Zou et al., 2013). Based on the GPS-TEC, geomagnetic field, ionosonde, and satellite observations, Tsurutani et al. (2004) showed that a large TEC enhancement occurs in low- and middle-latitude regions in association with the penetration of an intense convection electric field to the equatorial region during the main phase of the geomagnetic storm that occurred on 5–6 November 2001. They suggested that the TEC enhancement is caused by the “super fountain effect,” which is due to a large storm time electric field drift and ambipolar diffusion along the magnetic field line. Tsurutani et al. (2004) also pointed out that the higher-latitude part of the increased plasma density in the midlatitude is eroded by the expansion of the two-cell convection during the main phase of the geomagnetic storm. Kelley et al. (2004) proposed that the same TEC enhancement mechanism for low- and middle-latitude regions is responsible for the formation of the SED plume. However, Rishbeth et al. (2010) pointed out that it takes longer than the plasma lifetime to transport the plasma in the meridional direction and suggested that local production is important for SED formation, rather than transport of highly dense plasma from lower latitudes. Based on ionospheric simulation results, Heelis et al. (2009) showed that the equatorward expansion of the two-cell convection drives poleward and upward flows to uplift the ionosphere to higher altitudes, where the chemical recombination is much slower due to a decrease in the neutral density. Foster et al. (2007) suggested that large westward plasma fluxes carried by a subauroral polarization stream (SAPS) (Foster & Burke, 2002) play an important role in the formation of the SED. Based on a two-dimensional GPS-TEC map and horizontal ion drift data measured by Defense Meteorological Satellite Program (DMSP) satellites, Coster et al. (2007) showed that the SED plumes can be observed not only in the American sector but also in the European and Russian sectors during geomagnetic storms and suggested that the basic SED plume generation mechanism is the westward transport of high-density ionospheric plasma due to the electric field of the SAPS. Based on a comparison between the GPS-TEC observations and Thermosphere Ionosphere Electrodynamic General Circulation Model (TIEGCM), Liu, Wang, Burns, Solomon, et al. (2016) showed that the vertical $\mathbf{E} \times \mathbf{B}$ drifts in the upper ionosphere play an important role in the SED formation, while neutral winds mainly contribute to the generation of SED in the lower F region. They also mentioned that the horizontal $\mathbf{E} \times \mathbf{B}$ drifts are essential for the transport of ionospheric plasmas from the dayside convection throat region to the polar cap to generate the TOI structure at the polar cap. Based on the GPS-TEC, Pocker Flat Incoherent Scatter Radar (PFISR), Super Dual Auroral Radar Network (SuperDARN) radar, and Active Magnetosphere and Planetary Electrodynamics Response Experiment observations for six geomagnetic storms between 2010 and 2013, Zou et al. (2014) also reported the importance of upward vertical flow due to the projection of northward electric field drifts in sunlit regions for the formation of SED. They also found that the SED plume collocates with either upward or downward field-aligned currents (FACs) but appears equatorward of the peak of the Region 1 FAC in the dusk convection cell. Moldwin et al. (2016) reviewed the recent observation results and possible generation mechanisms of plasmaspheric plume, SED plume, and equatorial plasma plume. Heelis (2017) and Coster et al. (2017) classified an SED phenomenon into the midlatitude broad SED with the large spatial feature and the SED plume that expands from a high-latitude portion of the broad SED toward higher latitudes near local noon.

Although several different generation mechanisms of the midlatitude broad SED and SED plume were proposed based on ground and satellite observations and simulation studies, it remains unclear which of the following mechanisms is the most important: (1) westward transport of high-density ionospheric plasmas by SAPS (Foster et al., 2007), (2) latitudinal expansion of the storm time-enhanced EIA (Kelley et al., 2004;

Table 1
Location of Magnetometer, Ionosonde, and IS Radar Stations Used in the Present Study

Station name	Instrument	Geographic latitude (deg)	Geographic longitude (deg)	Geomagnetic latitude (deg)	Geomagnetic longitude (deg)
Huancayo (HUA)	Magnetometer	−12.05	284.67	−2.28	357.36
Kourou (KOU)	Magnetometer	5.21	307.27	14.27	20.47
Austin	Ionosonde	30.40	262.30	38.81	28.01
Boulder	Ionosonde	40.00	254.70	47.64	37.97
Juliusruh	Ionosonde	54.60	13.40	53.96	99.36
Rome	Ionosonde	41.90	12.50	41.81	93.72
Jicamarca	IS radar	−11.95	283.13	−2.32	355.86

Tsurutani et al., 2004), (3) local upward electric field drifts (Liu, Wang, Burns, Solomon, et al., 2016; Zou et al., 2014), or (4) equatorward-blowing neutral wind (Anderson, 1976). Few of the previous studies using the global TEC map with high time and spatial resolutions showed when and where the TEC enhancements related to the midlatitude broad SED and SED plume begin to appear during geomagnetic storms. In addition, we cannot easily identify if the equatorial or midlatitude ionosphere is the origin of these SED phenomena because the enhanced two-cell convection expands to lower latitudes during the main phase of large geomagnetic storms ($Dst = -200$ to -400 nT). The aims of this study are to identify when and where the enhanced TEC region related to the midlatitude broad SED and SED plume starts to appear in association with the onset of a moderate geomagnetic storm that occurred on 27 and 28 September 2017 and to investigate the temporal and spatial evolutions of the enhanced TEC region during the development and decay of the geomagnetic storm using global TEC observations with high spatial resolutions together with the solar wind, IMF, geomagnetic indexes (AE and $SYM-H$), ionosonde, geomagnetic field, Jicamarca (JIC) incoherent scatter (IS), and SuperDARN radar data.

2. Observation Data and Analysis Method

2.1. Data Sets

In this study, we used 1-min OMNI data of the solar wind proton density, flow speed, B_y and B_z components of the IMF in geocentric solar magnetospheric coordinates provided by the National Aeronautics and Space Administration Coordinated Data Analysis Web (<https://cdaweb.sci.gsfc.nasa.gov/index.html/>), the AE index (World Data Center for Geomagnetism, Nose et al., 2015), and the $SYM-H$ index (Iyemori, 1990; Iyemori & Rao, 1996) provided by the World Data Center for Geomagnetism, Kyoto University (<http://wdc.kugi.kyoto-u.ac.jp/index.html>). To identify the geomagnetically quiet days of each month, we also referred to a list of geomagnetically quiet and disturbed days provided by the GFZ German Research Centre for Geosciences (<ftp://ftp.gfz-potsdam.de/pub/home/obs/kp-ap/quietdst/qdrecent.txt>).

The global TEC data used for this analysis were derived from Global Navigation Satellite System (GNSS) observation data in Receiver Independent Exchange (RINEX) format obtained from many regional GNSS receiver networks. The number of GNSS stations reached more than 8,600 in January 2019. These GNSS observation data were provided by the National Institute of Geographic and Forest Information (<ftp://igs.eng.ign.fr/pub/igs/data>), University Navstar Consortium (UNAVCO; <ftp://data-out.unavco.org/pub/rinex/obs>), Crustal Dynamics Data Information System (CDDIS; <ftp://cddis.gsfc.nasa.gov/pub/gps/data/daily>), Scripps Orbit and Permanent Array Center (SOPAC; <ftp://garner.ucsd.edu/pub/rinex>), REseau National GPS permanent (RENAG; <ftp://renag.unice.fr/data>), Système d'Observation du Niveau des Eaux Littorales (SONEL; <ftp://ftp.sonel.org/gps/data>), TrigNet Web Application in South Africa (<ftp://ftp.trignet.co.za>), Instituto Brasileiro de Geografia e Estatística (ftp://geoftp.ibge.gov.br/informacoes_sobre_posicionamento_geodesico/rbmc/dados), SWEPOS–Sweden (ftp://ftp-sweposdata.lm.se:21/Rinex-data/Rinex2/se_swepos_daily), Norwegian Mapping Authority (NMA; <ftp://ftp.statkart.no/rnx2/24hour/30sec>), Can-Net Virtual Reference Station Network (<ftp://gpsweb.can-net.ca/RINEX>), Red Argentina de Monitoreo Satelital Continuo (RMSAC) (<ftp://ramsac.ign.gob.ar>) (Piñón et al., 2018), and other global and regional data centers (a total of more than 50 data providers; Tsugawa et al., 2018; Shinbori et al., 2018).

To investigate the temporal variation of the $h_m F_2$ and $f_o F_2$ in the F_2 region of the midlatitude and low-latitude ionosphere during a geomagnetic storm, we analyzed ionogram data obtained from four ionosonde stations (Austin, Boulder, Juliusruh, and Rome). The location of these station is shown in Table 1. These ionogram

data were provided by Lowell GIRO Data Center (LGDC) (<https://ulcar.uml.edu/DIDBase/>). This website has been supported by the GIRO project (Reinisch & Galkin, 2011).

We also used 5-min average ion drift velocity data obtained from the JIC IS radar and 1-min data of the H component of the geomagnetic field obtained at the Huancayo (HUA) and Kourou stations to investigate the response of the equatorial ionosphere to a sudden change in the IMF direction. The JIC IS radar and geomagnetic field data were provided by the Madrigal Database (<http://jro-db.igp.gob.pe/madrigal/>) and INTERMAGNET (www.intermagnet.org), respectively. The detailed location of these radar and geomagnetic stations is shown in Table 1. Further, we used electric potential map data calculated with the SuperDARN Assimilative Mapping procedure (Cousins et al., 2013) to investigate the temporal and spatial variations of the high-latitude convection for solar wind and IMF changes. The potential map data and analysis software were provided by Virginia Tech (<http://vt.superdarn.org/tiki-index.php?page=ASCIIData>). Basics of SuperDARN and brief history of midlatitude SuperDARN were found in the review paper by Nishitani et al. (2019).

2.2. TEC Data Processing

The GPS satellites transmit two coherent signals in the L-band with 1,575.42 MHz (L1) and 1,227.60 MHz (L2) frequencies, respectively. Considering that the refractive index of ionized plasmas depends on the frequency of the electromagnetic waves, we calculated the TEC value from the carrier phase difference between L1 and L2. Although we can derive the TEC value from the difference in two pseudoranges (P1 and P2), the data accuracy is 2 orders of magnitude lower than that calculated using L1 and L2 (Jakowski et al., 1996). The TEC values I derived from the pseudorange and carrier phase are written by the following equations:

$$I_P = (P_1 - P_2)A - (b_r + b_s)A, \quad (1)$$

$$I_L = (L_1 - L_2)A - (\lambda_1 n_1 - \lambda_2 n_2 + b'_r + b'_s)A, \quad (2)$$

where $A = \frac{1}{40.3} \left(\frac{1}{f_2^2} - \frac{1}{f_1^2} \right)^{-1}$; λ_1 and λ_2 are carrier wavelength at frequencies f_1 and f_2 , respectively; n_1 and n_2 are initialization constant at frequencies f_1 and f_2 , respectively; and b_r , b_s , b'_r , and b'_s are receiver and satellite biases of the pseudorange and carrier phase, respectively. Because the TEC value derived from the carrier phase is a relative value, the absolute amount of TEC is unknown because of the integer cycle ambiguities, $\lambda_1 n_1$ and $\lambda_2 n_2$ in Equation 2. Therefore, to compensate the TEC value calculated using the carrier phases, we adjusted it to the level of the TEC value calculated using the two pseudoranges. However, because the TEC value obtained from the pseudoranges includes the instrumental biases, we need to estimate the instrumental biases to determine the absolute TEC value.

For the instrumental bias estimation, we applied the method proposed by Otsuka et al. (2002), which consists of two steps: (1) estimation of hourly TEC averages and interfrequency biases by weighted least squares fitting of the relative TEC value obtained from each GNSS station and (2) exclusion of the biases from the relative TEC values. A detailed description and the equation used for this procedure can be found in Otsuka et al. (2002). Finally, we converted the slant TEC value into the vertical value and mapped the thin-shell ionosphere at an altitude of 300 km. For this purpose, we set the maximum satellite zenith angle to 75° and created grid data of the absolute TEC with a time and spatial resolution of 30 s and $0.5^\circ \times 0.5^\circ$ in longitude and latitude, respectively. Figure 1a shows a two-dimensional map of the number of TEC data points in each grid at 01:00 on 27 September 2017. In this figure, most of the grids of TEC data includes one or two data points, but the Japanese, Hawaiian, and west American regions have more than 4 data points because the GNSS receivers are densely installed in these regions. Discontinuity of the TEC value associated with an increase of the TEC data points cannot be seen in these regions, as shown in Figure 1b. We also performed pixel smoothing with a boxcar window of $2.5^\circ \times 2.5^\circ$ for the TEC data in geographic latitude and longitude and converted these smoothed TEC data into netCDF-formatted data to analyze the TEC data using Space Physics Environment Data Analysis Software (SPEDAS; Angelopoulos et al., 2019) and Inter-university Upper atmosphere Observation NETWORK (IUGONET) data analysis software (UDAS; Tanaka et al., 2013). The original GNSS-TEC data are stored in a database managed by the Dense Regional and Worldwide International GNSS-TEC observation (DRAWING-TEC) project at the

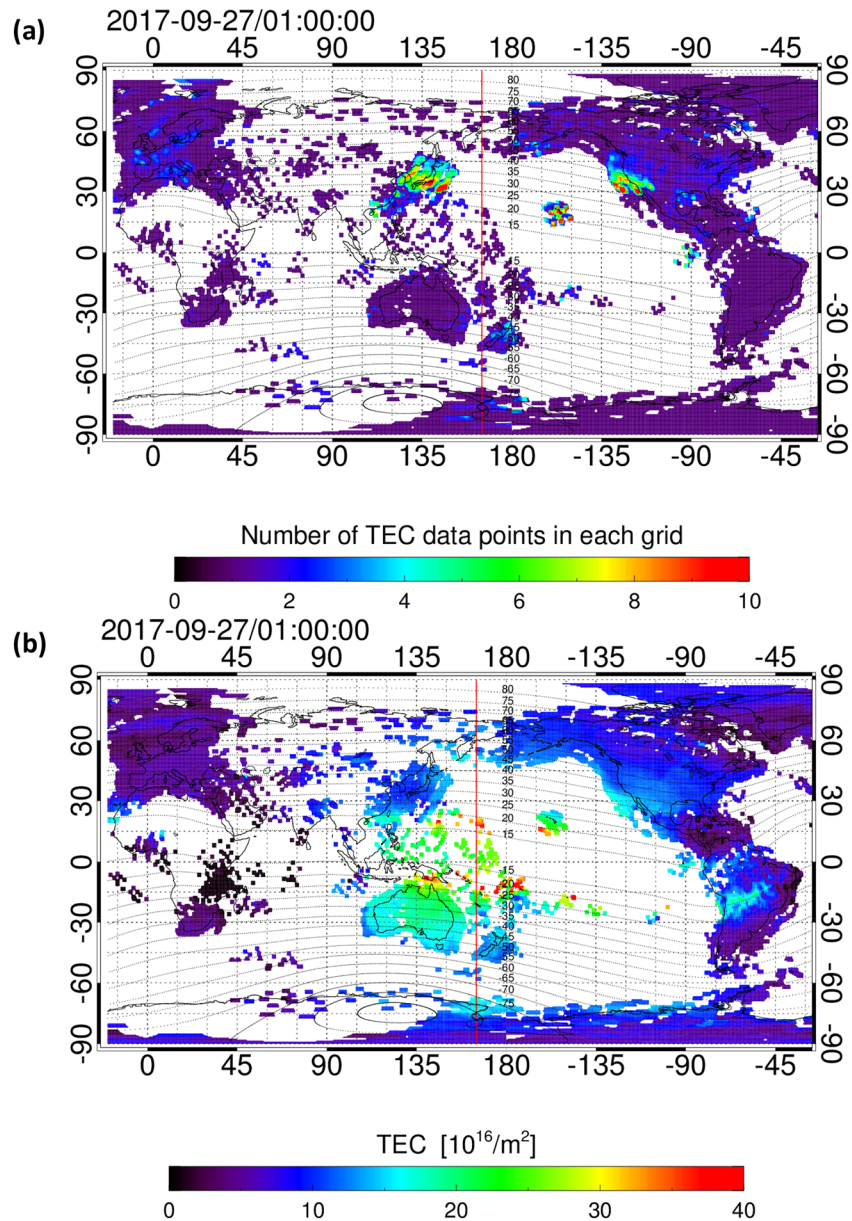


Figure 1. Two-dimensional maps of the number of TEC data points included in each $0.5^\circ \times 0.5^\circ$ longitude and latitude grid and the absolute TEC in geographic coordinates at 01:00 on 27 September 2017. The color codes indicate (a) the number of TEC data points and (b) the TEC value, respectively.

National Institute of Information and Communications Technology (NICT) (Tsugawa et al., 2007, 2018). In this study, we analyzed all 5-min GNSS-TEC data at the same spatial resolution to investigate the temporal and spatial variations of the midlatitude broad SED and SED plume and ionospheric electron density disturbances during a geomagnetic storm.

2.3. TEC Analysis Method

Because the electron density distribution in the ionosphere depends on the geographic latitude and longitude and local time, the TEC value also varies as a function of these parameters. Therefore, we must subtract the background TEC value under geomagnetically quiet conditions to investigate the disturbed components of the TEC value during geomagnetic storms. We first calculated the average TEC value of 10 geomagnetically quiet days per month using a list of quiet and disturbed days. Subsequently, we subtracted the

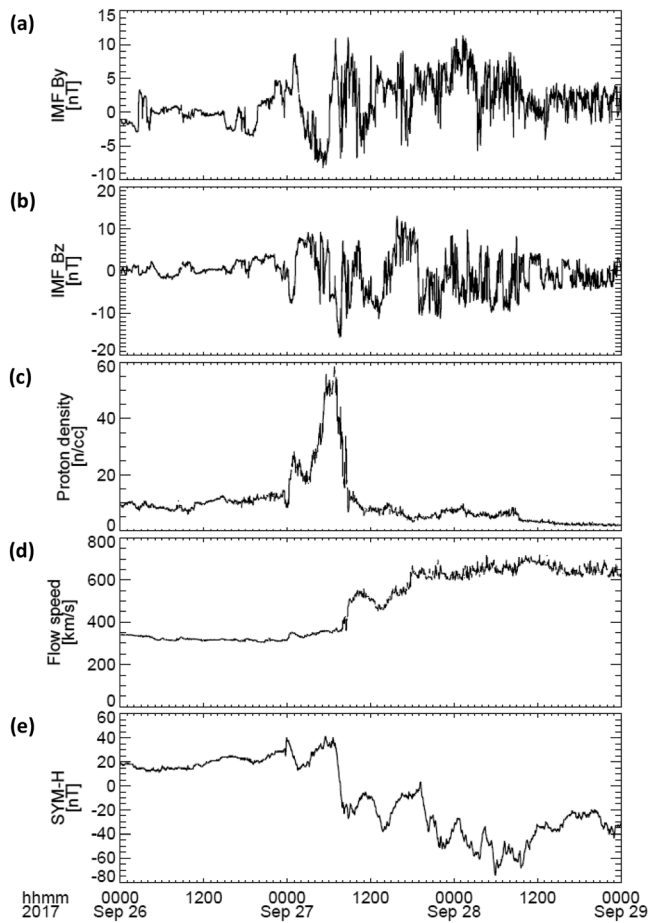


Figure 2. (a) IMF B_y , (b) IMF B_z , (c) solar wind proton density, (d) solar wind flow speed, and (e) $SYM-H$ index for the geomagnetic storm on 27–28 September 2017. The time interval is within a range of 3 days.

September. Corresponding to the arrival of solar wind disturbances in the Earth's magnetosphere, the $SYM-H$ value in Figure 2e decreases to -75 nT for approximately 1 day after the onset of a sudden commencement characterized by a sudden increase of the $SYM-H$ value at 00:00 UT on 27 September. Because the IMF direction changed from northward to southward and back many times, the $SYM-H$ index also decreases and increases corresponding to the timing of the IMF direction change.

3.2. Typical Example of SED Phenomena as Seen in a Two-Dimensional TEC Map

Figures 3b–3e show an example of two-dimensional maps of rTEC, TEC difference, and original TEC at 02:00 UT on 28 September during the main phase of the geomagnetic storm and the average TEC of 10 geomagnetic quiet days. In this case, the local noon indicated by the vertical red line is located at a geographic longitude of 150°E . In Figure 3b, the rTEC enhancement with a latitudinally narrow structure was observed in North America. The enhanced rTEC region expands to the high latitudes from 30°N to 70°N (geographic latitude) as local time varies from the evening (22:00) to the afternoon (14:00), which corresponds to an SED phenomenon. The latitudinal width becomes wider in the evening sector (18:00–22:00 local time, LT). The decreased rTEC region with a latitudinally narrow structure, which is identified as the midlatitude trough, appears at the higher latitude of the enhanced rTEC region. The other rTEC enhancement appears in the low-latitude and equatorial regions of South America from the evening (19:00) to midnight (24:00). This rTEC enhancement corresponds to the EIA phenomena. To check if the spatial structure of these rTEC enhancements seen in the rTEC is reliable, we compared the rTEC with TEC difference, storm time original TEC, and average TEC of 10 geomagnetic quiet days. As shown in Figures 3b–3d, a spatial structure of the SED, midlatitude trough, and EIA in the American sector does not almost change although colors are

average TEC value from the storm time TEC value and normalized the TEC difference using the absolute value of the average quiet-day TEC. In this study, we define the normalized TEC difference as the ratio of the TEC difference (rTEC). The above analysis method has been proposed by Immel and Mannucci (2013), but the definition of geomagnetically quiet time is different from the present study. Immel and Mannucci (2013) defined the geomagnetically quiet time as a period when the Dst index is more than -50 nT. Finally, we created two-dimensional maps of the normalized TEC difference in geographic and geomagnetic coordinates and a geographic latitude-time plot (keogram) of the rTEC in the American (280°E) sector to compare the rTEC variation with upward ion drift velocity obtained from the JIC IS radar. We used the Altitude-Adjusted Corrected Geomagnetic Model (AACGM) (Shepherd, 2014) to create the two-dimensional polar maps of rTEC in geomagnetic coordinates.

3. Characteristics of Temporal and Spatial Variations of the Ionosphere During a Geomagnetic Storm on 27–28 September 2017

3.1. Solar Wind Condition and Geomagnetic Activity

Figure 2 shows the 1-min IMF B_y and B_z components in geocentric solar magnetospheric coordinates, solar wind proton density, flow speed, and $SYM-H$ index during 26–29 September 2017. Figures 2c and 2d show that the solar wind proton density rapidly increases from 10 to 55/cc within 6–7 hr after 00:00 UT on 27 September. After the proton density decreases to less than 10/cc, the solar wind flow speed starts to increase from 350 to 700 km/s within 27 hr. This solar wind variation pattern is associated with the corotating interaction region, which is characterized by the transition from slow to fast solar winds. The IMF B_y and B_z components in Figures 2a and 2b show complex temporal variations with their amplitudes ranging from 7–10 nT after the onset of the solar wind proton density enhancement. The amplitude decreases after 12:00 UT on 28

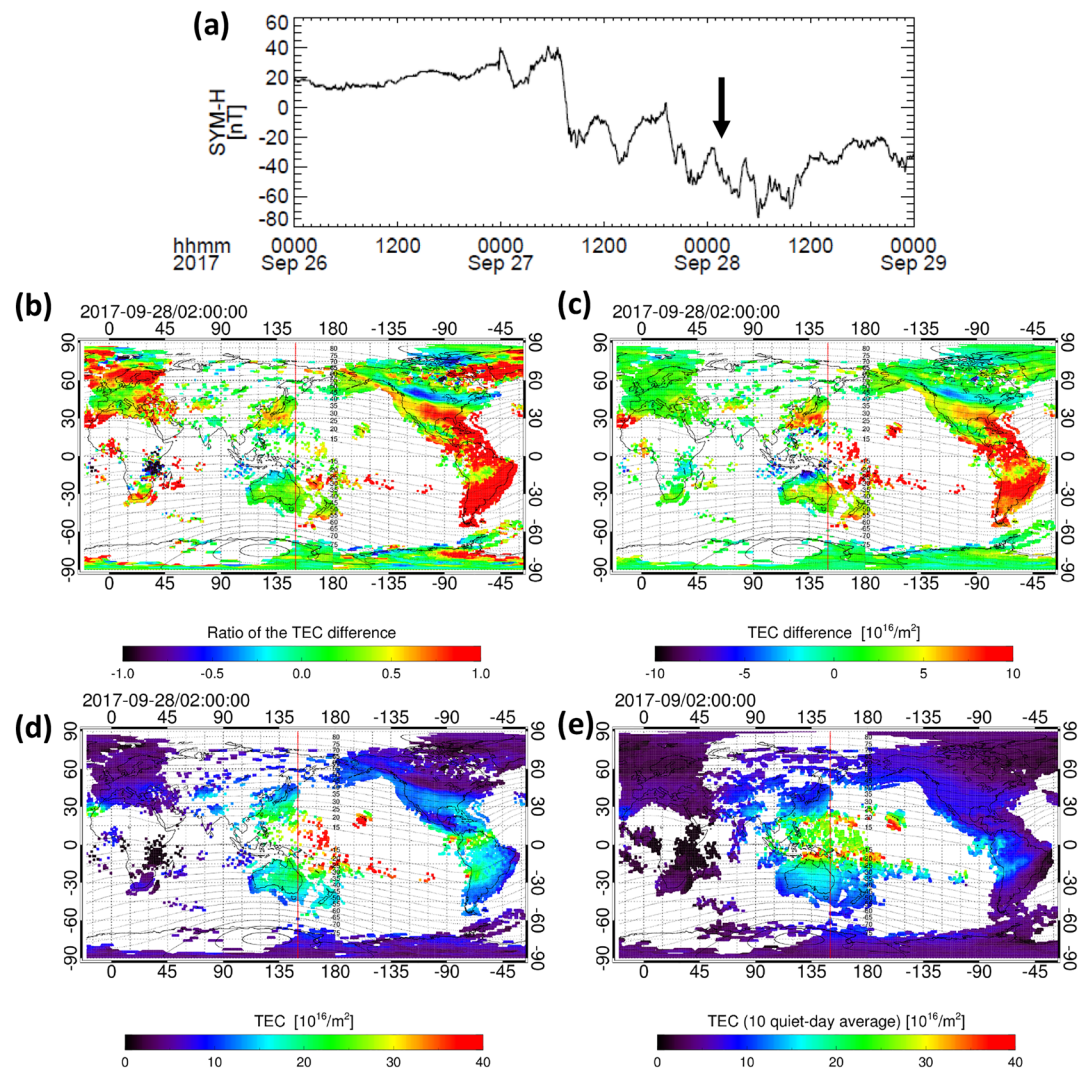


Figure 3. (a) *SYM-H* index, (b) ratio of the TEC difference between the storm time value and average value of 10 geomagnetically quiet days to the average value, (c) TEC difference, (d) storm time TEC, and (e) average TEC of 10 geomagnetically quiet days in September 2017. Time of two-dimensional maps in (b)–(d) is 02:00 UT on 28 September 2017. The vertical red line in each map indicates noon. The dashed lines correspond to the geomagnetic latitude at a height of 300 km calculated with the AACGM. The vertical arrow in (a) corresponds to the time of the two-dimensional TEC map.

different between each map. From this comparison, it is confirmed that the spatial structure of the storm time TEC variations is reliable as seen in the rTEC. Further, the rTEC map in the European and Greenland sectors can clearly capture the small TEC variations in the nighttime where the background TEC is also small (<5 TEC unit). Hereafter, we will discuss the temporal and spatial variations of the rTEC enhancement and depression during the geomagnetic storm.

3.3. Temporal and Spatial Variations of the rTEC Enhancements in the European and American Sectors

We found the clear rTEC enhancements in the daytime middle- and low-latitude regions around 08:00 UT and 20:00 on 27 September after an increase of the *AE* index and a decrease of the *SYM-H* index during this geomagnetic storm. The first and second rTEC enhancements occurred over Europe and North America, respectively. In this subsection, we describe the characteristics of temporal and spatial evolutions of these rTEC enhancements in the different longitudinal sector and find a common feature of their ionospheric responses to the geomagnetic storm.

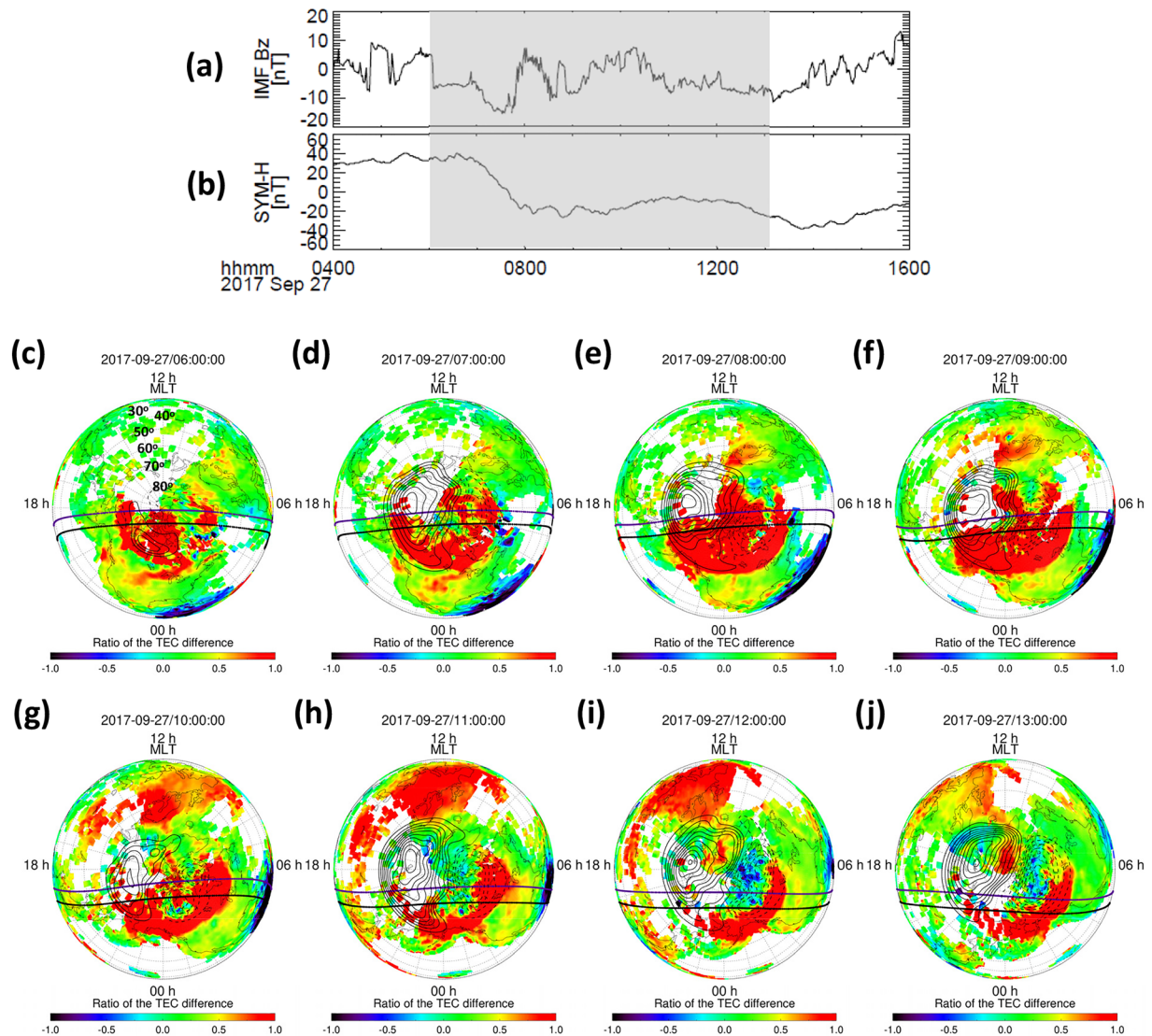


Figure 4. (a) IMF B_z , (b) $SYM-H$ index, and (c)–(j) two-dimensional polar maps of rTEC in geomagnetic coordinates for every hour from 06:00 to 13:00 UT on 27 September 2017. The shaded area in (a) and (b) corresponds to the period of the two-dimensional polar maps of rTEC in (c)–(j). The black and purple solid curves in (c)–(j) indicate the day-night terminators at a height of 300 and 105 km, respectively. The contour lines show the electric potential calculated with the SuperDARN assimilative mapping (SAM) procedure. The positive and negative potentials correspond to the dashed and solid lines, respectively. The number in (c) indicates the geomagnetic latitude calculated with the AACGM.

3.3.1. SED Phenomena Observed in the European Sector

Figure 4 shows the variations of the IMF B_z and $SYM-H$ index and two-dimensional polar maps of rTEC in the Northern Hemisphere in geomagnetic coordinates. In each polar map, the electric potential contour calculated with the SuperDARN Assimilative Mapping procedure (Cousins et al., 2013) is overplotted to find a change in the high-latitude convection pattern associated with the IMF B_z variations. The positive and negative potentials are indicated by the dashed and solid lines, respectively. The black and purple horizontal curves indicate a day-night terminator at a height of 105 and 300 km, respectively. In Figure 4d, the high-latitude convection is enhanced significantly and expands to the lower latitudes after the southward turning of the IMF at 06:06 UT, compared with that in Figure 4c. In Figure 4e, a significant rTEC enhancement first appears in the daytime high-latitude region (50–71°N [geomagnetic latitude: GMLAT] and 9:00–12:00 [magnetic local time, MLT]) at 08:00 UT, approximately 1 hr after an intensification of the southward IMF and start of the $SYM-H$ decrease. Later, the enhanced rTEC region expands to the GMLAT and MLT directions over time as shown in Figures 4f–4i. The enhanced rTEC region reached the low latitude

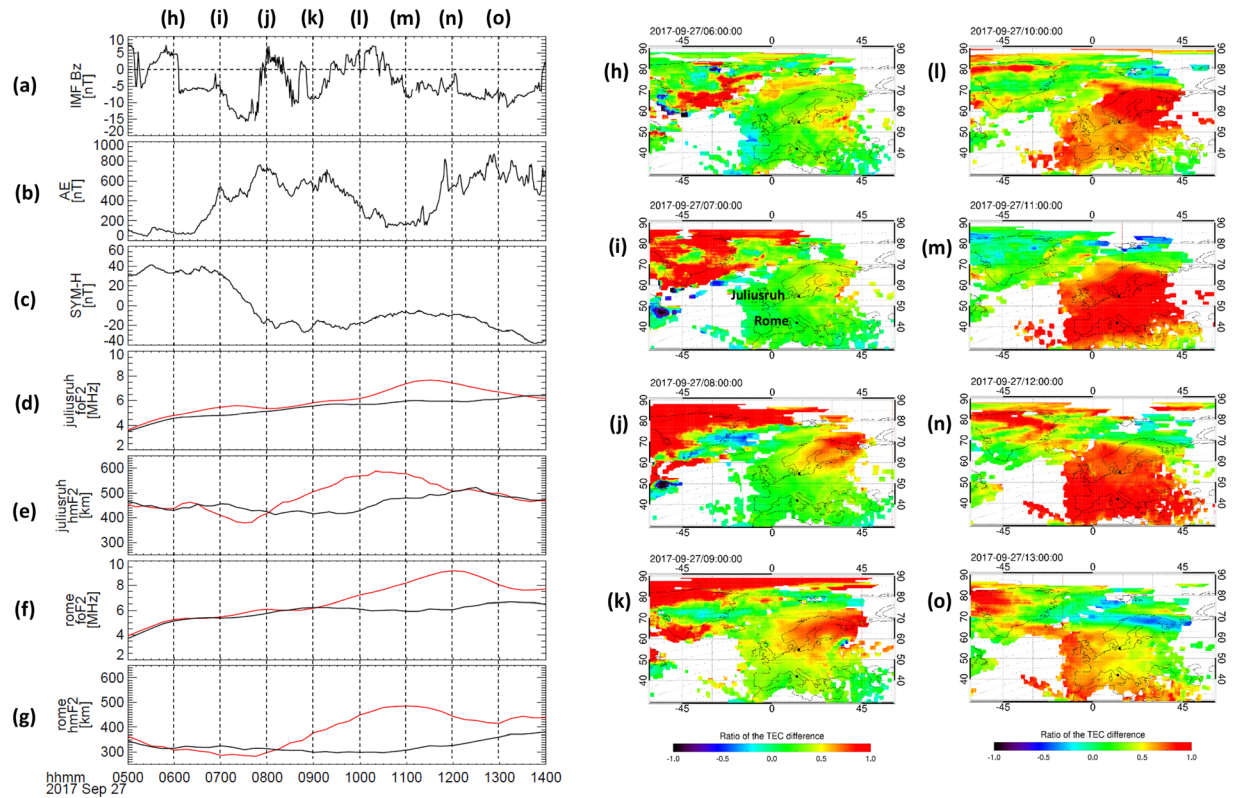


Figure 5. (a) IMF B_z , (b) AE index, (c) SYM-H index, (d) f_oF_2 at Juliusruh, (e) h_mF_2 at Juliusruh, (f) f_oF_2 at Rome, (g) h_mF_2 at Rome, and (h–o) two-dimensional maps of rTEC in the European sector in geographic coordinates for every hour from 06:00 to 13:00 UT on 27 September 2017. The red and black curves in (d)–(g) show the h_mF_2 and f_oF_2 values during this geomagnetic storm and a geomagnetically quiet time on 26 September, respectively. The black circles in the rTEC maps indicate the locations of the ionosonde stations shown in the left panels.

of $\sim 20^\circ\text{N}$ (GMLAT) within 2 hr after an appearance of the initial rTEC enhancement. In Figure 4h, the region with the rTEC value of more than 0.5 (corresponding to the yellow color) is observed at least in wide GMLAT and MLT ranges of $20\text{--}70^\circ\text{N}$ (GMLAT) and $09:00\text{--}21:00$ (MLT), respectively, although the ground GNSS-TEC observation is not covered enough in the Russian and Ocean regions. This rTEC enhancement with a wide latitudinal and longitudinal extent corresponds to the midlatitude broad SED (Coster et al., 2017). As shown in Figure 4g, the high-latitude convection is weakened and shrunk in association with the northward turning of the IMF, but the extension of the enhanced rTEC region is not ceased. This feature indicates that the rTEC enhancement is not only caused by a convection electric field. This point will be discussed in section 4. In Figures 4i and 4j, the rTEC enhancement with a narrow structure appears in the high-latitude region ($>60^\circ\text{N}$ GMLAT) at $11:00\text{--}12:00$ (MLT), which is separated from the latitudinally broad rTEC enhancement. This structure corresponds to the SED plume defined by Coster et al. (2017). The enhanced rTEC region expands to the polar cap, which corresponds to the TOI. In Figure 4j, the SED plume and TOI seem to be distributed along the electric potential contours of the dusk convection cell. Further, the rTEC depression with a latitudinally narrow structure also appears in the daytime sector ($13:00\text{--}17:00$ MLT) along the dusk convection cell. This structure corresponds to the midlatitude trough.

In order to understand a change of the ionospheric electron density structure related to the midlatitude broad SED during this geomagnetic storm, we analyzed the temporal variation of f_oF_2 and h_mF_2 derived from the ionosonde data at the two latitudinally separated points. The result is shown in Figure 5 (left). The location of the two ionosonde stations (Juliusruh and Rome) is indicated by the black circles in each two-dimensional rTEC map of the European sector. In Figures 5d–5g, the black line shows the f_oF_2 and h_mF_2 values during a geomagnetically quiet days (26 September). After the southward excursion of the IMF B_z , the AE index showed a significant increase up to ~ 700 nT, which indicates that the high-latitude ionospheric currents are enhanced in association with an increase of auroral activity and high-latitude

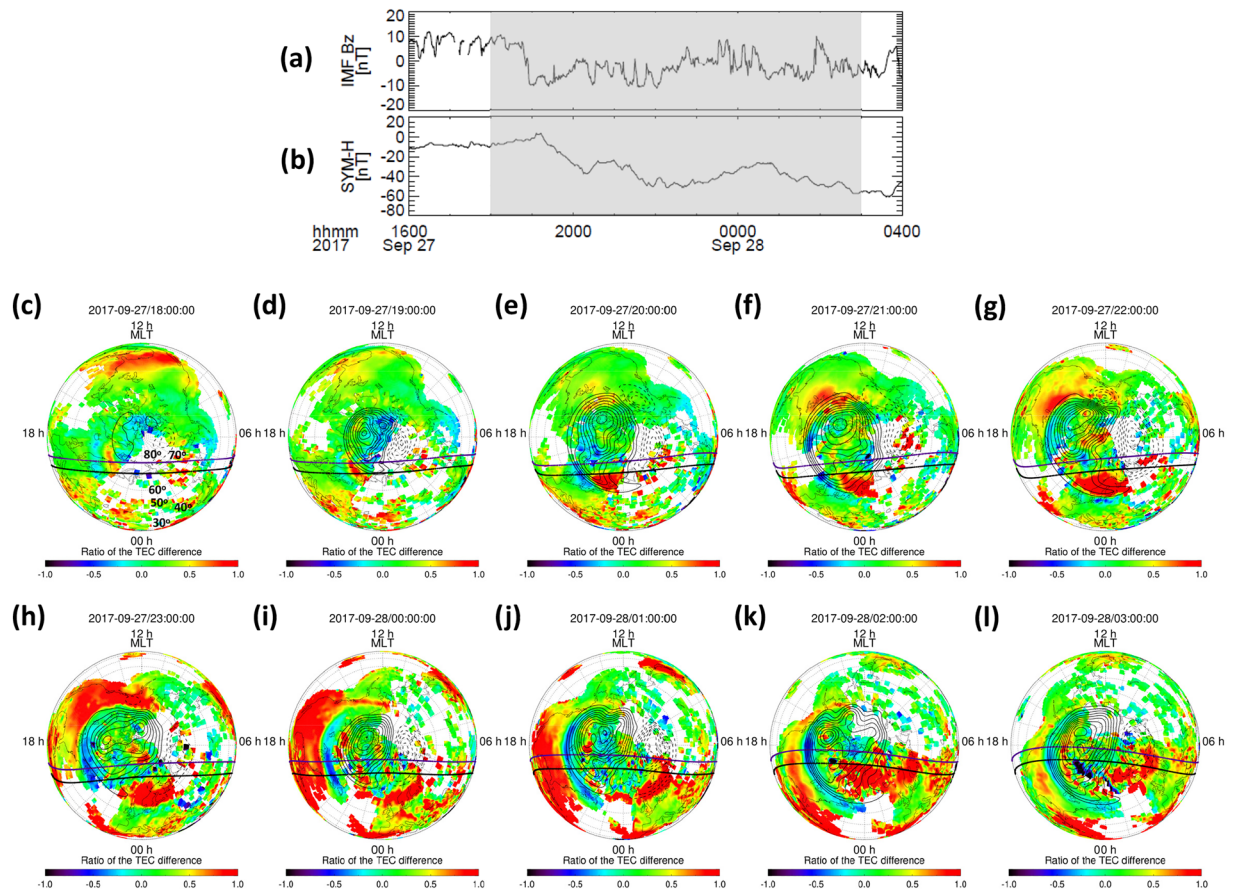


Figure 6. (a) IMF B_z , (b) SYM- H index, and (c–l) two-dimensional polar maps of rTEC in geomagnetic coordinates for every hour from 18:00 on 27 September to 02:00 UT on 28 September 2017. The format of this figure is the same as that of Figure 4.

convection. The $h_m F_2$ values at both the stations decrease from 470 to 380 km and from 320 to 290 km during 6:20–07:40 UT, respectively, in association with the increasing AE index and southward IMF. After that, the $h_m F_2$ values increase from 380 to 590 km and from 290 to 490 km. The increasing periods of the $h_m F_2$ values at the high- and low-latitude stations are from 07:40 to 10:20 UT and from 07:40 to 11:00 UT, respectively. This implies that the timing of the increasing $h_m F_2$ values is almost simultaneous between the two stations, but the time when the $h_m F_2$ value at the low latitude becomes maximum is delayed for 40 min. Based on the increasing height and period of the F_2 region of the ionosphere, we can estimate the average upward velocities of the ionospheric plasmas at the Juliusruh and Rome stations as approximately 21.9 and 16.7 m/s, respectively. This result indicates that the average upward velocity at the high latitude is a little faster than that at the low latitude. The $f_o F_2$ values increased with 1- to 2-hr delay from the onset time of the $h_m F_2$ increase. Before the $f_o F_2$ values become maximum, the $h_m F_2$ values begin to decrease. Comparing the $f_o F_2$ and $h_m F_2$ variations with the two-dimensional rTEC maps, one cannot see the clear rTEC enhancement over the ionosonde stations during a decrease of the height of the F_2 region and just after the onset of an increase of the height. Approximately 1 hr after the increasing height of the F_2 region of the ionosphere, the rTEC value begins to increase over the high- and low-latitude stations, but the increasing rate of the rTEC is larger over the high-latitude station than that over the low-latitude one as shown in Figure 5k. Finally, the rTEC values are enhanced significantly in a wide latitudinal range as seen in Figures 5l–5n. In Figure 5o, the rTEC values show a decrease to ~ 0.5 over both the stations, corresponding to a decrease of the $f_o F_2$ values shown in Figures 5d and 5f.

3.3.2. SED Phenomena Observed in the American Sector

Figure 6 shows the variations of the IMF B_z and SYM- H index and two-dimensional polar maps of rTEC in the Northern Hemisphere in geomagnetic coordinates. The format of this figure is the same as that of

Figure 4. After the southward turning of the IMF B_z at 18:55 UT, the high-latitude convection is intensified significantly and expands to the midlatitude region, as shown in Figures 6d and 6e. The $SYM-H$ index in Figure 6b also shows a gradual decrease to -52 nT, which indicates that a ring current is developed in the inner magnetosphere in association with an enhancement of the magnetospheric convection. In Figure 6e, the rTEC enhancement first appears in the afternoon high- and middle-latitude regions ($50\text{--}70^\circ\text{N}$ [GMLAT], 12:00–15:00 [MLT]) approximately 1 hr after the high-latitude convection enhancement associated with the negative excursion of the IMF B_z . The initial rTEC enhancement is observed in the westward convection region of the equatorward dusk cell as shown in Figure 6c. After 20:00, the IMF B_z shows large fluctuations with its amplitude of 5–10 nT and sometimes has a positive value. During this period, the high-latitude convection pattern shows a complicated structure in each polar map (Figures 6e–6l), but the intensity remains larger, compared with that during the stable northward IMF (Figure 6c). As shown in Figures 6f–6i, the rTEC enhancement expands to the GMLAT and MLT directions in the equatorward dusk convection cell over time. This signature almost resembles the pattern of the rTEC enhancement observed in the European sector. At 23:00 UT, another rTEC enhancement appears in the low-latitude of the evening sector (17:00–20:00 [MLT]), and this structure merges with the middle- and low-latitude enhanced rTEC region as shown in Figure 6i. The rTEC enhancement in the evening low-latitude region corresponds to the EIA phenomenon. At 00:00 UT on 28 September, the rTEC enhancement shows a latitudinally narrow structure in the afternoon high-latitude region ($60\text{--}70^\circ\text{N}$ [GMLAT] and 12:00–15:00 [MLT]), which is separated from the midlatitude broad rTEC enhancement. This rTEC enhancement corresponds to the SED plume (e.g., Coster et al., 2017). After 01:00 UT, the rTEC enhancement observed in the American sector gradually decays with time. In Figures 6h–6l, the decreased rTEC region with a latitudinally narrow structure is formed at the higher latitude of the midlatitude enhanced rTEC region. This rTEC structure corresponds to the midlatitude trough. Particularly, in Figures 6k and 6l, the intervals of the electric potential contour of the dusk convection cell becomes narrower along the midlatitude trough. This potential drop corresponds to the SAPS electric field, which creates a fast westward plasma flow equatorward of the dusk convection cell (e.g., Coster et al., 2017; Foster et al., 2007).

To investigate the temporal variation of the ionospheric electron density structure during this geomagnetic storm in the American sector as well as in the European sector shown in Figure 5, we analyzed the f_oF_2 and h_mF_2 values obtained from the two ionosonde stations (Boulder and Austin). The result is shown in Figure 7. The format of this figure is the same as that of Figure 5. After the southward turning of the IMF at 18:55 UT, the AE and $SYM-H$ indexes show a significant increase and decrease within a few of hours. These signatures indicate the enhancements of the ionospheric currents and auroral activity at high latitudes and ring current in the inner magnetosphere associated with an increase of the high-latitude convection shown in Figure 6. In Figure 7e, the h_mF_2 value at the Boulder station in the midlatitude region begins to increase around 19:00 UT and reaches the maximum height of 630 km at 22:50 UT. The f_oF_2 value also begins to increase at 20:50 UT and becomes maximum at 00:00 UT on 28 September. The h_mF_2 value begins to decrease before the f_oF_2 value becomes maximum. In Figure 7g, the h_mF_2 value at the Austin station in the low-latitude region begins to increase around 20:00 UT and reaches the maximum height of 550 km at 22:00 UT. The h_mF_2 value begins to decrease around 23:00 UT before the f_oF_2 value becomes maximum as shown in Figure 7f. In this case, the onset time of the increasing height of the F_2 region of the ionosphere is delayed at the low-latitude station, compared with that at the midlatitude station. Comparing the temporal variation of these ionospheric parameters with the rTEC distribution in the American sector, we find that the rTEC enhancement begins to occur at 20:00 UT in the midlatitude region around -90°E in geographic longitude and the h_mF_2 value at the Boulder station shows a gradual increase. At this time, the clear rTEC enhancement cannot be recognized over the Boulder station, as shown in Figure 7i. Also in Figure 7j, the clear rTEC enhancement cannot yet be seen over the Boulder and Austin stations although the h_mF_2 values becomes larger, compared with those of the quiet time level. After 22:00 UT, the significant rTEC enhancement occurs over both the ionosonde stations shown in Figures 7k–7o. During this period, the f_oF_2 values at both the ionosonde stations show a significant enhancement, as seen in Figures 7d and 7f. In these rTEC maps, the EIA begins to develop after 21:00 or 22:00 UT, and this structure merged with the midlatitude rTEC enhancement as shown in Figures 7j–7o. The appearance of the enhanced EIA is delayed significantly from the onset of the negative excursion of the IMF B_z or the enhancement of high-latitude convection shown in Figure 6.

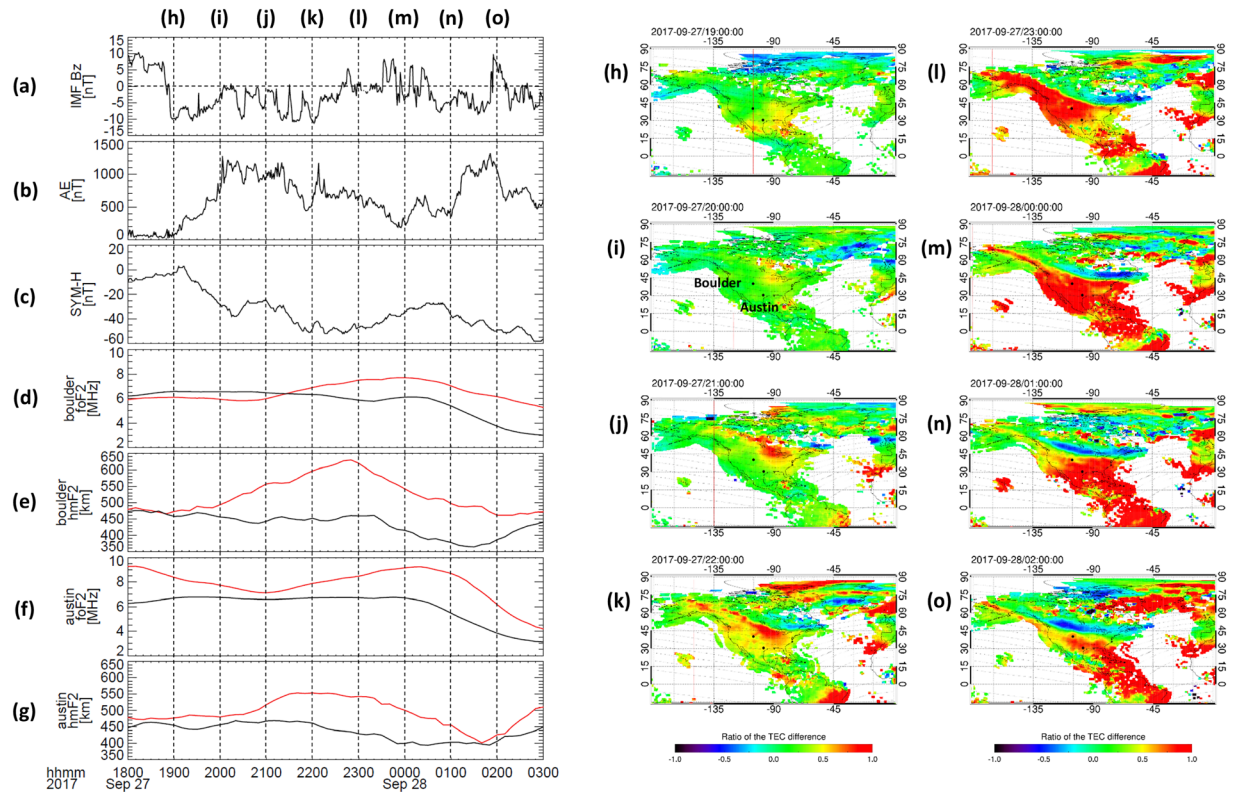


Figure 7. (a) IMF B_z , (b) AE index, (c) SYM-H index, (d) f_oF_2 at Boulder, (e) h_mF_2 at Boulder, (f) f_oF_2 at Austin, (g) h_mF_2 at Austin, and (h–o) two-dimensional maps of rTEC in the American sector in geographic coordinates for every hour from 18:00 UT on 27 September to 04:00 UT on 28 September 2017. The format of this figure is the same as that of Figure 5.

3.3.3. Response of the Equatorial Ionosphere to Prompt Penetration Electric Field in the American Sector

Figures 6 and 7 show a clear enhancement of the EIA in the equatorial and low-latitude regions of the evening American sector during the geomagnetic storm. In this subsection, we investigate the response of the equatorial ionosphere to the prompt penetration electric field using the JIC IS radar, geomagnetic field, and rTEC observation data. Figure 8 shows the B_z component of the IMF, AE and SYM-H indexes, the height profile of vertical ion drift velocity observed at the JIC IS radar, the difference of the H component of the geomagnetic field (dH) at the HUA and Kourou stations, and the geographic latitude-time plot of the rTEC along the geographic longitude of 280° (-80°E) in the time interval from 05:00 on 27 September to 05:00 on 28 September. The horizontal dashed line shown in Figure 8f indicates the dip equator at a height of 300 km. The three vertical dashed lines give the onset times of a sudden increase of the AE index. At 06:25 UT on 27 September, the vertical ion drift velocity and dH show a negative excursion within a few of minutes after the onset time of the enhancement of the AE index. At this time, the JIC and HUA stations are located at 01:25 LT, corresponding to the postmidnight sector. These signatures indicate that the westward polar electric field penetrates to the nighttime equatorial ionosphere and the westward electric field drives the westward ionospheric current that leads to a negative excursion of dH . In Figure 8f, the rTEC value near the dip equator shows a significant depression within 10 min after the sudden enhancement of the westward electric field in the equatorial region. After that, the vertical ion drift velocity in Figure 8d shows a sudden positive excursion at 08:00 UT and a further increase up to more than 50 m/s after 09:00 UT associated with a positive excursion of the B_z component of the IMF. The dH tends to increase in association with a positive excursion of the upward ion drift velocity. This result implies that the eastward electric field penetrates to the equatorial ionosphere in association with the northward turning of the IMF. After the second enhancement of the AE index at 11:17 UT on 27 September, the dH shows a short-lived increase with a time scale of 2–3 hr corresponding to the period of the southward IMF and decrease of the SYM-H

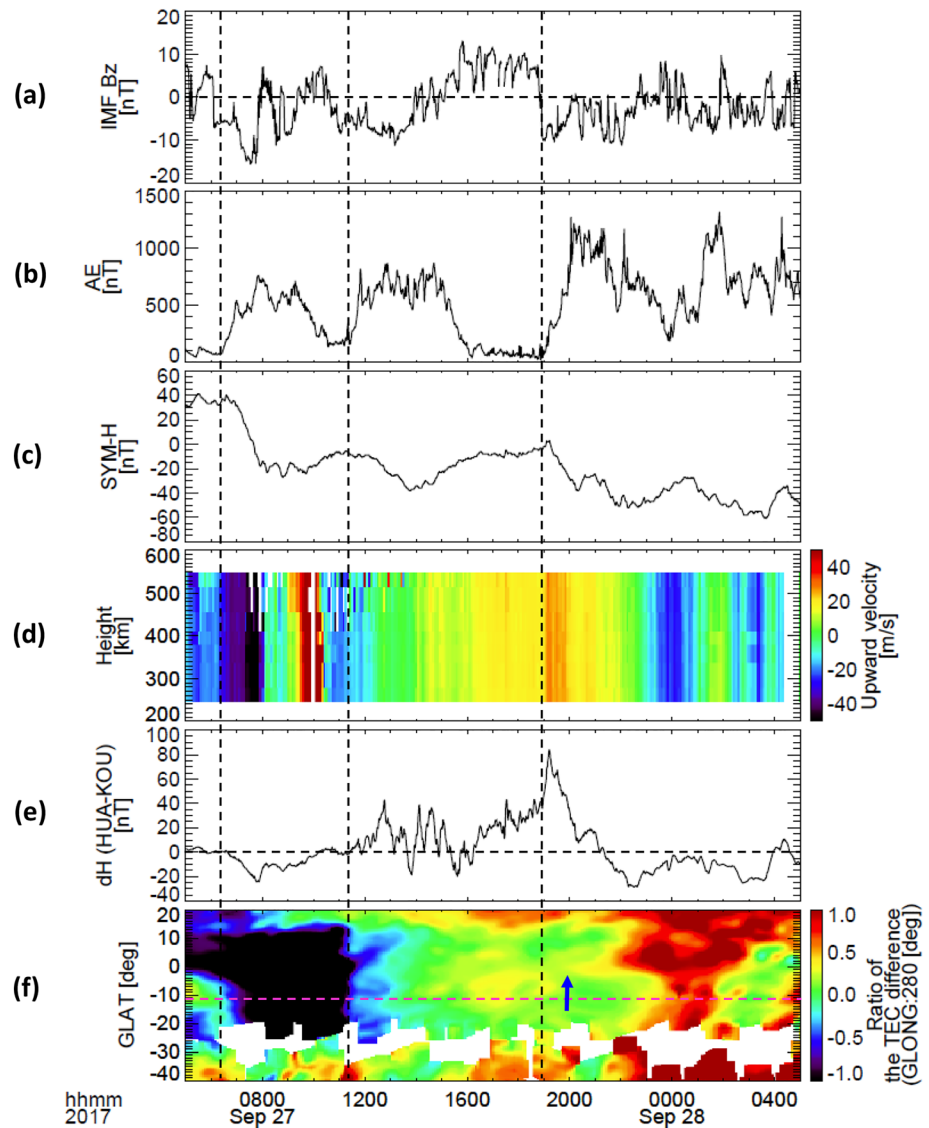


Figure 8. (a) IMF B_z , (b) AE index, (c) SYM-H index, (d) height profile of upward (vertical) ion drift velocity observed by the Jicamarca IS radar, (e) difference value of the H component of the geomagnetic field (dH) between the Huancayo and Kourou stations, (f) geographic latitude-time plot of rTEC along the geographic longitude (280°E) in time interval from 05:00 on 27 September to 05:00 on 28 September 2017. The dashed pink line in (f) indicates the dip equator. The three vertical dashed lines correspond to the onset times of a sudden increase of the AE index.

value. The vertical ion drift velocity also shows a positive excursion corresponding to the dH enhancement. At this time, the JIC and HUA stations are located in the morning sector (06:00–09:00 LT). After 12:30 UT, the dH shows the fluctuations with their amplitude and period of 20–30 nT and 30–40 min, respectively. Corresponding to the positive variations of the dH , the vertical ion drift velocity shows a short-lived enhancement in Figure 8d. The rTEC value shows a sudden increase with a wide latitudinal range in association with the second enhancement of the AE index or the dH increase. The clear rTEC variation cannot be seen in the GMLAT-time plot for the dH and ion drift velocity fluctuations observed during 12:30–16:00 UT. After the third enhancement of the AE index and the depression of the SYM-H index associated with the southward excursion of the B_z component of the IMF at 18:55 UT, the vertical ion drift velocity and dH shows a sudden increase within a few of minutes. In this case, the JIC and HUA stations are located in the afternoon sector (14:00 LT). These signatures indicate that the eastward electric field penetrates to the equatorial ionosphere and causes an enhancement of the eastward equatorial

electrojet current that produces a positive magnetic field variation on the ground. Approximately 1 hr after the onset of the upward ion drift velocity and dH enhancements, the rTEC enhancement appears at 20:00 UT in the Northern Hemisphere with respect to the dip equator, indicated by the blue arrow in Figure 8f, and this structure expands to the higher latitude within 3–4 hr as the rTEC value is enhanced significantly. During this rTEC enhancement, the vertical ion drift velocity and dH decrease with time, and their values are changed from positive to negative after 21:00 UT. Furthermore, corresponding to the largely negative excursion of the vertical ion drift velocity from 23:00 UT on 27 September to 01:00 UT on 28 September, the rTEC value near the dip equator is enhanced significantly. At this time, the JIC and HUA stations are located in the evening sector (18:00–20:00 LT). This negative excursion of the vertical ion drift velocity corresponds to the periods of the northward IMF, decreasing AE index, and increasing $SYM-H$ index in Figures 8a–8c, respectively.

4. Discussion

The present global TEC data analyses showed that the rTEC enhancements first appeared at the high latitudes of the noon or afternoon sector within 1 hr after an enhancement and expansion of the high-latitude convection associated with the southward IMF. The enhanced rTEC region tended to rapidly expand to the low latitudes with a wide MLT direction with some delay from an appearance of the initial rTEC enhancement. In the case of the rTEC enhancement observed in the European sector, the enhanced rTEC regions existed in wide GMLAT and MLT ranges of 20–70°N and 09:00–18:00, respectively, as shown in Figure 4. Further, a latitudinally narrow rTEC enhancement separated from the midlatitude broad rTEC enhancement appeared at the high latitudes from the noon to afternoon sectors. The rTEC enhancements with the latitudinally broad and narrow structures correspond to the midlatitude broad SED and SED plume, respectively, defined by Heelis (2017) and Coster et al. (2017). In the afternoon sector, the decreased rTEC region was observed with a latitudinally narrow structure at the higher latitudes of the SED and SED plume. This structure corresponds to the midlatitude trough that is collocated with the SAPS flow (Foster & Burke, 2002) as shown in Figures 6k and 6l. In fact, the interval of the electric potential contour became narrower inside the decreased rTEC region equatorward of the dusk convection cell, compared with that in other regions as shown in Figures 4j, 6f, 6g, 6k, and 6l. This result suggests a significant potential drop associated with the SAPS electric field, which produces a westward fast plasma flow in the subauroral region. This feature of the evolution of the rTEC enhancement was commonly seen in both the European and American sectors. Later, in the American sector, another rTEC enhancement in the equatorial and low-latitude regions related to the EIA appeared in the evening sector (17:00–20:00 MLT) and expanded to the higher latitudes as shown in Figures 6h and 6j. Finally, the equatorial rTEC enhancement merged with the midlatitude rTEC enhancement at the low latitudes as seen in Figures 6j and 6h.

By analyzing the temporal and spatial evolutions of the rTEC variations in detail introduced by Immel and Mannucci (2013), we found that the midlatitude broad SED is generated by a low-latitude expansion of the enhanced rTEC region at the high latitudes. In order to understand the generation mechanism of the low-latitude expansion of the rTEC enhancement, we analyzed the ionosonde data obtained from the midlatitude and low-latitude stations in the Europe and American sectors. As a result, the $h_m F_2$ value at all the stations increased after a sudden enhancement of the high-latitude convection associated with the southward excursion of the IMF. This signature represents an upward motion of the F_2 region of the ionosphere. The onset time of the $h_m F_2$ variation was almost simultaneous between the midlatitude and low-latitude stations in the European sector, but it was delayed at the low latitude in the American sector as shown in Figures 5 and 7. Further, the upward velocity of the F_2 region of the ionosphere was a little faster at the midlatitude than at the low latitude in the European sector. Thus, in this study, it was shown that the onset time of the upward motion of the F_2 region of the ionosphere and its velocity were different between the midlatitude and low-latitude regions. Approximately 1–2 hr after the ionospheric plasmas in the F_2 region began to move upward, the $f_o F_2$ and rTEC values showed a significant enhancement in both the midlatitude and low-latitude regions as shown in Figures 5 and 7. The time when the $f_o F_2$ value became maximum was delayed at the low latitudes. The delay of the $f_o F_2$ enhancement from the onset time of the upward motion of the F_2 region implies that it takes a few of hours for the newly produced ionospheric plasmas to uplift at the higher latitude, where the recombination rates are smaller when the production persists at the lower

latitude in the sunlit region shown in the simulation result by David et al. (2011). These $h_m F_2$ and $f_o F_2$ signatures during the geomagnetic storm is almost consistent with those reported by Dashora et al. (2009) and Galav et al. (2014), who investigated the response of the F_2 region of the ionosphere to the geomagnetic storm that occurred on 15 May 2005 using only one ionosonde station at the low latitude or midlatitude. The present study newly showed that the response of the F_2 region of the ionosphere to the geomagnetic storm is delayed at the low latitudes by analyzing the ionosonde data obtained from several stations. From the above discussion, it can be interpreted that the equatorward expansion of the midlatitude rTEC enhancement is due to the delay of the electron density enhancement at the low latitudes by the local production of the ionospheric plasma in the sunlit region.

Many previous studies on the response of the magnetosphere, ionosphere, and thermosphere associated with solar wind disturbances and geomagnetic storms using ground-based and satellite observations and simulation have been conducted (e.g., Aa et al., 2019; Astafyeva et al., 2016; Blanc & Richmond, 1980; Bruinsma & Forbes, 2007; David et al., 2011; Ferdousi et al., 2019; Huang, 2008; Kikuchi et al., 1996, 2008; Liu, Wang, Burns, Yue, et al., 2016; Liu, Wang, Burns, Solomon, et al., 2016; Nishida, 1968; Sori et al., 2019; Tanaka, 1995; Tanaka et al., 2016). According to previous knowledge, when the southward IMF arrives at the magnetopause and the merging process between the IMF and geomagnetic field occurs at the dayside magnetopause, the solar wind energy effectively enters the magnetosphere and the intensity of FACs and high-latitude convection is enhanced significantly. The enhanced polar electric field penetrates to the dayside and nightside low-latitude and equatorial ionosphere and distributes in the inner magnetosphere (Kikuchi, 2014; Kikuchi & Hashimoto, 2016). The penetration electric field is directed eastward and westward in the daytime and nighttime, respectively, and drives the ionospheric currents with the same direction as that of the electric field at the equator. The equatorial ionospheric current causes the enhancement and depression of the H component of the geomagnetic field (Abdu et al., 2007; Tsuji et al., 2012). When the intensity of the southward IMF suddenly weakens or a northward turning of the IMF takes place, the intensity of R1 FACs and convection electric field decreases rapidly, and the R2 FACs and shielding electric field relatively becomes larger in the midlatitude to equatorial ionosphere and inner magnetosphere (e.g., Kikuchi et al., 2003, 2008; Tsuji et al., 2012). In the present study, the high-latitude convection and auroral electrojet were enhanced rapidly in association with the southward IMF, and the eastward and westward electric fields penetrated to the dayside and nightside equatorial ionosphere, as shown in Figure 8. From a comparison between the variations of the vertical ion drift velocity in the postmidnight equatorial ionosphere and the $h_m F_2$ at the morning midlatitude and low-latitude ionosphere in Figures 4 and 8, the onset time of both the variations is almost coincident. From this result, it can be interpreted that these ionospheric variations are caused by prompt penetration electric field to the midlatitude to equatorial ionosphere associated with a sudden enhancement of the high-latitude convection. Further, the sign of the $h_m F_2$ variation at the middle and low latitudes of the European sector changed from negative to positive during the significant enhancement of the downward motion of the equatorial ionosphere in the postmidnight sector (1:00–3:00 LT). This result suggests that the zonal component of the convection electric field turned from westward to eastward in the morning sector as reported by Ebihara et al. (2014). Therefore, we can consider that the upward and downward motions of the middle- and low-latitude ionosphere of the European sector are caused by the enhanced convection electric field associated with the southward IMF. Further, based on the upward average velocity calculated with the $h_m F_2$ variation at the two ionosonde stations, we can estimate the zonal component of the electric field as approximately 2.8 and 1.4 mV/m in the middle- and low-latitude regions, respectively. The latitudinal variation of the magnitude of the zonal component of the electric field suggests that the source of the electric field is located in the polar region. From the above discussion based on the rTEC, $h_m F_2$, $f_o F_2$, and vertical ion drift velocity observations, it can be considered that a major cause of the equatorward expansion of the midlatitude broad SED observed in the European sector is due to the spatial distribution of the convection electric field intensity, which leads to the spatial difference of an upward motion and production of the F_2 region of the ionosphere in the sunlit region.

After the formation of the midlatitude broad SED, the SED plume with a latitudinally narrow structure was formed along the electric potential contour of the dusk convection cell as shown in Figures 4 and 6. The rTEC enhancement related to the SED plume extended from the throat region between the dawn and dusk convection cells to the polar cap region as seen in Figures 4i and 4j. In this case, the throat region was not located just at the noon but at the prenoon (10:00–11:00 MLT) associated with the clockwise rotation of

the high-latitude convection pattern. Friis-Christensen et al. (1985) reported that a spatial distribution of the horizontal equivalent currents derived from the Greenland magnetometer data is changed by the direction of the B_y and B_z components of the IMF. According to their results, the pattern of the equivalent currents related to the high-latitude convection showed a clockwise rotation for all the cases of the IMF B_y pattern under the negative value of the IMF B_z . Recently, Nakamizo and Yoshikawa (2019) clarified that the deformation of the high-latitude convection pattern is established by the combined effects of the solar wind and ionospheric polarization due to the spatial inhomogeneity of ionospheric conductivities with the use of an electric potential solver (Nakamizo et al., 2012). In this study, it was newly shown that the SED plume can expand from the afternoon or evening sector to the prenoon sector and move toward the high-latitude region from the throat region between the dawn and dusk convection cells due to the clockwise rotation of the high-latitude convection pattern. Although Yizengaw et al. (2006) reported that the SED plume was observed over the European region of the morning sector (10:30–12:00 LT), they did not interpret that the formation of the prenoon SED plume is formed by the high-latitude convection pattern. Recently, Heelis (2017) pointed out that a shape of the ionospheric convection trajectory is important to form the SED plume. The present data analysis result is basically consistent with the suggestion by Heelis (2017). Therefore, based on the above discussion, it can be considered that the structure of the SED plume strongly depends on the high-latitude convection pattern. According to Nakamizo and Yoshikawa (2019), since the spatial distribution of the high-latitude convection depends on both the solar wind and ionospheric conductivities, the statistical feature of the SED plume will be established by a statistical analysis in future studies.

Recently, Ferdousi et al. (2019) reported that a significant enhancement of the equatorward natural wind occurred in the high- and middle-latitude regions with several-hour delay of an increase of the sunward SAPS flow associated with a geomagnetic storm that occurred on 17 March 2013 using DMSP-18 and Gravity Field and Steady-State Ocean Circulation Explorer (GOCE) satellite observations. This time difference is almost consistent with our observational results. Ferdousi et al. (2019) also showed that the electron density enhancement appeared in the daytime (10:00–16:00 MLT) midlatitude region ($50\text{--}60^\circ$ GMLAT) in the results of the physics-based Rice Convection Model-Coupled Thermosphere, Ionosphere, Plasmasphere, electrodynamics (RCM-CTIPE) simulation. They interpreted the reason as a transportation of ionospheric plasmas to a higher altitude where the recombination rate is low by the equatorward neutral wind (e.g., Prölss, 1997). Figures 4g, 5, and 8 show that the h_mF_2 value at 10:00 UT on 27 September continued to increase in spite of the decreasing high-latitude convection and the enhancement of the eastward electric field in the equatorial ionosphere of the predawn sector associated with the northward turning of the IMF. This observational fact indicates that the overshielding electric field originating from the R2 FACs penetrates to the midlatitude to equatorial ionosphere associated with a sudden decrease of the R1 FACs (e.g., Kikuchi et al., 2003, 2008). Because the overshielding electric field contributes to the downward motion of the daytime ionospheric plasmas to the lower altitude, where the recombination rates is larger, the increasing h_mF_2 and f_oF_2 values cannot be explained by an effect of the shielding electric field. Considering the results reported by Ferdousi et al. (2019), there is a possibility that the equatorward natural wind in the thermosphere flows in the subauroral and midlatitude regions. Therefore, it can be considered that the equatorward neutral wind gives some contributions to the upward motion of the middle- and low-latitude ionosphere. This detailed point should be solved in future studies.

As shown in Figures 6–8, the h_mF_2 value in the midlatitude of the American sector also began to increase after the enhancement of the high-latitude convection associated with the southward IMF. The enhanced convection electric field penetrated to the equatorial ionosphere. Because the onset time of the increasing h_mF_2 value almost coincided with that of the significant enhancement of the high-latitude convection electric field, a major cause of the increasing h_mF_2 value in the midlatitude can be considered as the upward motion of the F_2 region of the ionosphere due to the enhanced convection electric field. Approximately 1–2 hr after the onset of the increasing h_mF_2 value, the f_oF_2 and $r\text{TEC}$ values began to increase in association with the production of the F_2 region of the ionosphere in the sunlit region. However, the h_mF_2 value in the low latitude began to increase with several hours of delay from that in the midlatitude although the enhanced convection electric field penetrated to the equatorial ionosphere as shown in Figure 8. In this case, because half a day passed from the start of the geomagnetic storm, it can be considered that the meridional neutral wind blowing from the Southern to Northern Hemispheres suppresses the upward motion of the ionospheric plasmas due to the enhanced convection electric field. This point should be solved in future studies.

Further, we showed that the EIA was intensified in the evening sector (17:00–20:00 MLT) and merged with the enhanced rTEC structure in the midlatitude and low latitude, as seen in Figures 6 and 7. The intensification of the EIA started with 1-hr delay from the onset of the enhancements of the upward motion of the F_2 region of the ionosphere and eastward equatorial electrojet current as shown in Figure 8. From a comparison between Figures 6 and 8, this onset time almost corresponds to the start time of the midlatitude rTEC enhancement related to the midlatitude broad SED. The enhanced equatorial rTEC region expanded to the higher latitude within 3–4 hr. This time scale is almost consistent with the development of the EIA reported by Rastogi and Klobouchar (1990) and Balan and Iyer (1983). The signatures of the equatorial ionosphere and equatorial electrojet current indicate that the eastward electric field penetrates to the low-latitude equatorial ionosphere in association with an enhancement of the high-latitude convection due to the southward IMF (e.g., Dashora et al., 2009, 2019; Tsurutani et al., 2004). Dashora et al. (2009) showed that the low-latitude TEC enhancements are caused by the local effect of the prompt penetration of the electric field during the main phase of the geomagnetic storm event that occurred on 15–16 May 2005. Further, Dashora et al. (2019) statistically established the local effect of the prompt penetration of the electric field on the equatorial TEC enhancements during the main phase of 37 geomagnetic storms. Therefore, based on the results in Figure 8 and previous work, it can be thought that the occurrence of the rTEC enhancement in the equatorial region and higher-latitude expansion is also caused by the local upward motion and production of the F_2 region of the ionosphere in the sunlit region due to the prompt penetration of the electric field to the equator and fountain effect. Although the rTEC enhancement cannot be clearly seen near the dip equator associated with an enhancement of upward motion of the ionosphere, it is caused by the depression of the electron density due to the enhanced upward plasma motion around the magnetic equator (Heelis & Coley, 2007; Tsurutani et al., 2004). In this event, the vertical ion drift velocity showed a gradual decrease, and the sign was changed around 23:00 UT on 27 September, as shown in Figure 8d, in association with a decrease of the southward IMF intensity or the northward turning of the IMF. The ion drift velocity had a minimum value of -30 m/s at 00:00 UT on 28 September. This signature suggests that the electric field was reversed and enhanced significantly near the local time when the prereversal enhancement usually occurs (e.g., Fejer, 1991). In this case, it can be considered that the overshielding electric field is intensified significantly due to the conductivity gradient near the day-night terminator. In Figures 8d and 8f, the clear enhancement of the rTEC can be seen around the dip equator with correspondence to the enhancement of the over-shielding electric field. The rTEC enhancement can be interpreted as a suppression of the decrease of the electron density due to the reverse electric field, compared with that during a geomagnetically quiet time.

Based on the above discussion, we can propose the new story of the formation of the midlatitude to equatorial enhanced rTEC structure associated with geomagnetic storms as follows.

1. In association with an arrival of the southward IMF to the magnetosphere, the high-latitude convection is intensified significantly and expands to the low latitudes. The enhanced convection electric field penetrates to the equatorial ionosphere.
2. After the enhancement of the high-latitude convection and penetration of the electric field to the equator, the ionospheric plasmas from the midlatitude to the equatorial regions are carried upward by the electric field. The upward velocity depends on the spatial distribution of the electric field intensity.
3. Approximately 1–2 hr after the onset of the increase of the height of the F_2 region, the electron density begins to increase equatorward of the high-latitude convection cell if the production of the low-altitude F_2 region continues. The enhancement of the electron density begins at the high-latitude region where the upward velocity of the ionospheric plasmas is faster than that at the low latitudes, and the enhanced region expands to the low latitudes with a wide longitudinal extent within a few of hours. Thus, the midlatitude broad SED structure is formed.
4. After the appearance of the midlatitude broad SED structure, the rTEC enhancement related to the SED plume with a latitudinally narrow structure that is separated from the midlatitude broad SED is formed equatorward of the dusk convection cell or midlatitude trough. The SED plume extends from the afternoon or evening sector to the prenoon sector, depending on the high-latitude convection pattern. Further, the SED plume moves toward the high latitudes from the throat region between the dawn and dusk convection cells and enters the polar cap region as a TOI phenomenon.

Acknowledgments

This work was supported by JSPS KAKENHI Grants 26400478 and 16H06286 and the National Institute of Polar Research (NIPR) through General Collaboration Project 29-11. The coauthor (Y. O.) was also supported by MEXT/JSPS KAKENHI Grants 15H05815 and 16H05736. We took advantage of the IUGONET database (IUGONET Type-A) and data analysis software (UDAS). The solar wind, IMF, and PC index were provided by the National Aeronautics and Space Administration (NASA) Coordinated Data Analysis Web (CDAWeb) (<https://cdaweb.sci.gsfc.nasa.gov/index.html/>). We used geomagnetic indices (*AU*, *AL*, and *SYM-H*) with 1-min time resolution provided by the World Data Center (WDC) for Geomagnetism, Kyoto University (<http://wdc.kugi.kyoto-u.ac.jp/index.html>). We also referred to a list of geomagnetically quiet and disturbed days provided by the GFZ German Research Centre for Geosciences (<ftp://ftp.gfz-potsdam.de/pub/home/obs/kp-ap/quietdst/qdrecent.txt>). The GNSS data collection and processing were performed using the NICT Science Cloud. The Receiver Independent Exchange (RINEX) format data used for GNSS-TEC processing were provided by the following organizations: UNAVCO (<ftp://data-out.unavco.org>), DGRSDUT (<http://gnss1.tudelft.nl>), Arecibo Observatory (<http://www.naic.edu>), CDDIS (<ftp://cddis.gsfc.nasa.gov>), CHAIN (<ftp://chain.physics.unb.ca>), CORS (<ftp://www.ngs.noaa.gov>), GDAF (<ftp://geodaf.mt.asi.it>), BKG (<ftp://igs.bkg.bund.de>), IGS (<ftp://rgpdata.ign.fr>), EUOLG (<ftp://olggps.oew.ac.at>), Geoscience Australia (<ftp://ftp.ga.gov.au>), IGSIGN (<ftp://igs.eng.ign.fr>), KASI (<ftp://nfs.kasi.re.kr>), PNGA (<http://www.geodesy.cwu.edu>), IBGE (<ftp://geofp.ibge.gov.br>), RGCL (<ftp://ftp.itacyl.es>), TNG (<ftp://196.15.132.3>), SOPAC (<ftp://garner.ucsd.edu>), NRC (<ftp://wcda.pgc.nrcan.gc.ca>), GEONET (<ftp://163.42.5.1>), HRAO (<ftp://geoid.hartrao.ac.za>), GRN (<ftp://rinex.smartnetna.com>), GNNZ (<ftp://ftp.geonet.org.nz>), RENAG (<ftp://renag.unice.fr>), SONEL (<ftp://ftp.sonel.org>), FRDN (<ftp://www.crs.inogs.it>), LINZ (<ftp://apps.linz.govt.nz>), ROB (<ftp://gnss.oma.be>), GOP (<ftp://ftp.pecny.cz>), RGE (<ftp://62.99.86.141>), RGNA (<ftp://geodesia.inegi.org.mx>), CENAT (<ftp://ramsac.ign.gob.ar>), INGv (<ftp://bancadati2.gm.ingv.it>), REP (<ftp://158.49.61.10>), SWSBM (<ftp://ftp-out.sws.bom.gov.au>), CORS (<ftp://meristemum.carm.es>), AFREF (<ftp://ftp.afrefdata.org>), WHU (<ftp://igs.gnsswhu.cn>), TLALOCNET (<ftp://tla-locnet.udg.mx>), NCEDC (<ftp://www.ncedc.org>), ODT (<ftp://ftp.odot.state.or>

5. Also in the equatorial region, approximately 1 hr after the prompt penetration of the electric field to the equator, the rTEC enhancement appears off the dip equator by an enhanced equatorial fountain, and the enhanced rTEC region expands to the higher latitude within 3–4 hr.
6. The enhanced EIA structure merges with the midlatitude broad SED at the low latitudes through the local vertical **ExB** drift and equatorial fountain effect due to the prompt penetration of the electric field to the low-latitude and equatorial ionosphere.

5. Conclusions

To investigate the temporal and spatial evolutions of the TEC enhancement and electron density in the ionosphere from high-latitude to equatorial regions during a geomagnetic storm that occurred on 27 and 28 September 2017, we analyzed global GNSS-TEC data with high time and spatial resolutions (5 min) and geographic latitudes and longitudes of $0.5^\circ \times 0.5^\circ$ together with the solar wind, IMF, geomagnetic indexes (*Kp*, *AE*, and *SYM-H*), geomagnetic field, ionosonde, JIC IS radar, and SuperDARN radar data. As a result, the clear rTEC enhancement related to the midlatitude broad SED first occurs from noon to afternoon at high latitudes within 1 hr after a sudden increase and expansion of the high-latitude convection and prompt penetration of the electric field to the equator associated with the southward excursion of the IMF. Approximately 1–2 hr after the onset of the h_mF_2 increase in the midlatitude and low-latitude regions associated with the high-latitude convection enhancement, the rTEC and f_oF_2 values begin to increase and the enhanced rTEC region expanded to the low latitudes within 1–2 hr. This signature suggests that the ionospheric plasmas in the F_2 region move at a higher altitude due to local electric field drift, where the recombination rate is smaller, and that the electron density increases due to additional production at the lower altitude in the sunlit region. In the European sector, the average vertical electric field drift velocity of the ionosphere is a little faster at the midlatitude than that at the low latitude. This result implies that the electric field intensity tends to increase with an increasing latitude and that the source of the electric field is located at high latitudes. After the appearance of the midlatitude broad SED, the SED plume with a latitudinally narrow structure is separated from the midlatitude broad SED and is formed along the dusk convection cell or equatorward of the midlatitude trough, indicating an rTEC depression with a latitudinally narrow structure. The SED plume can expand up to the prenoon sector (10:00–11:00 MLT) due to the clockwise rotation of the high-latitude convection pattern. The SED plume moves toward the high latitudes from the throat region between the dawn and dusk convection cells and enters the polar cap region as a TOI phenomenon. Later, another rTEC enhancement related to the EIA appears in the equatorial region approximately 1 hr after the prompt penetration of the electric field to the equator and expands to higher latitudes within 3–4 hr. The structure of the rTEC enhancement merges with the midlatitude broad SED structure at the low latitude.

References

Aa, E., Zou, S., Ridley, A., Zhang, S., Coster, A. J., Erickson, P. J., et al. (2019). Merging of storm time midlatitude traveling ionospheric disturbances and equatorial plasma bubbles. *Space Weather*, *17*, 285–298. <https://doi.org/10.1029/2018SW002101>

Abdu, M. A., Maruyama, T., Batista, I. S., Saito, S., & Nakamura, M. (2007). Ionospheric responses to the October 2003 superstorm: Longitude/local time effects over equatorial low and middle latitudes. *Journal of Geophysical Research*, *112*, A10306. <https://doi.org/10.1029/2006JA012228>

Anderson, D. N. (1976). Modeling the midlatitude F-region ionospheric storm using east-west drift and a meridional wind. *Planetary and Space Science*, *24*(1), 69–77. [https://doi.org/10.1016/0032-0633\(76\)90063-5](https://doi.org/10.1016/0032-0633(76)90063-5)

Angelopoulos, V., Cruce, P., Drozdov, A., Grimes, E. W., Hatzigeorgiu, N., King, D. A., et al. (2019). The Space Physics Environment Data Analysis System (SPEDAS). *Space Science Reviews*, *215*(1), 9. <https://doi.org/10.1007/s11214-018-0576-4>

Astafeyeva, E., Zakharenkova, I., & Alken, P. (2016). Prompt penetration electric fields and the extreme topside ionosphere response to the June 22–23, 2015, geomagnetic storms as seen by the swarm constellation. *Earth, Planets and Space*, *68*(1), 152. <https://doi.org/10.1186/s023-016-0526-x>

Balan, N., Alleyne, H., Otsuka, Y., Vijaya, L. D., Fejer, B. G., & McCrea, I. (2009). Relative effects of electric and neutral wind on positive ionospheric storms. *Earth Planets, Space*, *61*(4), 439–445. <https://doi.org/10.1186/BF03353160>

Balan, N., & Iyer, K. N. (1983). Equatorial anomaly in ionospheric electron content and its relation to dynamo currents. *Journal of Geophysical Research*, *88*(A12), 10,259–10,262. <https://doi.org/10.1029/JA088iA12p10259>

Balan, N., Shiokawa, K., Otsuka, Y., Kikuchi, T., Vijaya Lekshmi, D., Kawamura, S., et al. (2010). A physical mechanism of positive ionospheric storms at low latitudes and midlatitudes. *Journal of Geophysical Research*, *115*, A02304. <https://doi.org/10.1029/2009JA014515>

Blanc, M., & Richmond, A. (1980). The ionospheric disturbance dynamo. *Journal of Geophysical Research*, *85*, 1669–1686. <https://doi.org/10.1029/JA085iA04p01669>

us), SWEPOS (<ftp://ftp-sweposdata.lm.se>), EUREF (<ftp://www.epncb.oma.be>), IGG (<ftp://ftp.glonass-iac.ru>), SUGAUR (<ftp://eos.ntu.edu.sg>), NMA (<ftp://ftp.statkart.no>), NERC (<ftp://128.243.138.204>), RAMSAC (<ftp://ram-sac.ign.gob.ar>), and ERGNSS (<ftp://ftp.geodesia.ign.es>). The SuperDARN electric potential map data and analysis software were provided by Virginia Tech (<http://vt.superdarn.org/tiki-index.php?page=ASCIIData>). SuperDARN is a collection of radars funded by the national scientific funding agencies of Australia, Canada, China, France, Italy, Japan, Norway, South Africa, the United Kingdom, and the United States of America. The ion drift velocity data obtained from the Jicamarca IS radar are provided by the Madrigal Database (<http://jro-db.igp.gob.pe/madrigal/>). The Jicamarca Radio Observatory is a facility of the Instituto Geofísico del Perú operated with support from NSF AGS-1433968 through Cornell University. We used the 1-min geomagnetic field data collected at Huancayo and Kourou. We thank Instituto Geofísico del Perú and Institut de Physique du Globe de Paris for supporting its operation and INTERMAGNET for promoting high standards of magnetic observatory practice (www.intermagnet.org). We also analyzed ionogram data obtained from four ionosonde stations (Austin, Boulder, Juliusruh, and Rome). These ionogram data were provided by Lowell GIRO Data Center (LGDC) (<https://ulcar.uml.edu/DIDBase/>). The Juliusruh ionosonde has been operated by the Leibniz Institute of Atmospheric Physics Kuehlungsborn.

Bruinsma, S. L., & Forbes, J. M. (2007). Global observation of traveling atmospheric disturbances (TADs) in the thermosphere. *Geophysical Research Letters*, *34*, L14103. <https://doi.org/10.1029/2007GL030243>

Buonsanto, M. J. (1995a). Millstone Hill incoherent scatter *F* region observations during the disturbances of June 1991. *Journal of Geophysical Research*, *100*(A4), 5743–5755. <https://doi.org/10.1029/94JA03316>

Buonsanto, M. J. (1995b). A case study of the ionospheric storm dusk effect. *Journal of Geophysical Research*, *100*(A12), 23,857–23,869. <https://doi.org/10.1029/95JA02697>

Buonsanto, M. J. (1999). Ionospheric storms: A review. *Space Science Reviews*, *88*(3/4), 563–601. <https://doi.org/10.1023/A:1005107532631>

Coster, A. J., Colerico, M. J., Foster, J. C., Rideout, W., & Rich, F. (2007). Longitude sector comparisons of storm enhanced density. *Geophysical Research Letters*, *34*, L18105. <https://doi.org/10.1029/2007GL030682>

Coster, A. J., Erickson, P. J., Foster, J. C., Thomas, E. G., Ruohoniemi, J. M., & Baker, J. (2017). Solar cycle 24 observations of storm-enhanced density and the tongue of ionization. In T. Fuller-Rowell, E. Yizengaw, P. H. Doherty, & S. Basu (Eds.), *Ionospheric space weather: Longitude and hemispheric dependences and lower atmosphere forcing*, *Geophysical Monograph*, *220*, (pp. 71–83). Washington, DC: American Geophysical Union.

Coster, A. J., Foster, J. C., & Erickson, P. J. (2003). Monitoring the ionosphere with GPS. *GPS world*, *14*, 40.

Cousins, E. D. P., Matsuo, T., & Richmond, A. D. (2013). SuperDARN assimilative mapping. *Journal of Geophysical Research: Space Physics*, *118*, 7895–7904. <https://doi.org/10.1002/2013JA019319>

Dashora, N., Sharma, S., Dabas, R. S., Alex, S., & Pandey, R. (2009). Large enhancements in low latitude total electron content during 15 May 2005 geomagnetic storm in Indian zone. *Annales de Geophysique*, *27*(1803–1820), 2009.

Dashora, N., Suresh, S., & Niranjana, K. (2019). Interhemispheric asymmetry in response of low-latitude ionosphere to perturbation electric fields in the main phase of geomagnetic storms. *Journal of Geophysical Research: Space Physics*, *124*, 7256–7282. <https://doi.org/10.1029/2019JA026671>

David, M., Sojka, J. J., Schunk, R. W., Liemohn, M. W., & Coster, A. J. (2011). Dayside midlatitude ionospheric response to storm time electric fields: A case study for 7 September 2002. *Journal of Geophysical Research*, *116*, A12302. <https://doi.org/10.1029/2011JA016988>

Ebihara, Y., Tanaka, T., & Kikuchi, T. (2014). Counter equatorial electrojet and overshielding after substorm onset: Global MHD simulation study. *Journal of Geophysical Research: Space Physics*, *119*, 7281–7296. <https://doi.org/10.1002/2014JA020065>

Evans, J. V. (1973). The causes of storm-time increases of the *F*-layer at mid-latitudes. *Journal of Atmospheric and Solar - Terrestrial Physics*, *35*(4), 593–616. [https://doi.org/10.1016/0021-9169\(73\)90191-8](https://doi.org/10.1016/0021-9169(73)90191-8)

Fejer, B. G. (1991). Low latitude electrodynamic plasma drifts: A review. *Journal of Atmospheric and Terrestrial Physics*, *53*(8), 677–693. [https://doi.org/10.1016/0021-9169\(91\)90121-M](https://doi.org/10.1016/0021-9169(91)90121-M)

Ferdousi, B., Nishimura, Y., Maruyama, N., & Lyons, L. R. (2019). Subauroral neutral wind driving and its feedback to SAPS during the 17 March 2013 geomagnetic storm. *Journal of Geophysical Research: Space Physics*, *124*, 2323–2337. <https://doi.org/10.1029/2018JA026193>

Foster, J. C. (1993). Storm-time plasma transport at middle and high latitudes. *Journal of Geophysical Research*, *98*(A2), 1675–1689. <https://doi.org/10.1029/92JA02032>

Foster, J. C., & Burke, W. J. (2002). SAPS: A new characterization for sub-auroral electric fields. *Eos, Transactions, American Geophysical Union*, *83*(36), 393–394. <https://doi.org/10.1029/2002EO000289>

Foster, J. C., Coster, A. J., Erickson, P. J., Holt, J. M., Lind, F. D., Rideout, W., et al. (2005). Multiradar observations of the polar tongue of ionization. *Journal of Geophysical Research*, *110*, A09S31. <https://doi.org/10.1029/2004JA010928>

Foster, J. C., Rideout, W., Sandel, B., Forrester, W. T., & Rich, F. J. (2007). On the relationship of SAPS to storm enhanced density. *Journal of Atmospheric and Solar-Terrestrial Physics*, *69*(3), 303–313. <https://doi.org/10.1016/j.jastp.2006.07.021>

Friis-Christensen, E. A., Kamide, Y., Richmond, A. D., & Matsushita, S. (1985). Interplanetary magnetic field control of high latitude electric fields and currents determined from Greenland magnetometer data. *Journal of Geophysical Research*, *90*(A2), 1325–1338. <https://doi.org/10.1029/JA090iA02p01325>

Galav, P., Rao, S. S., Sharma, S., Gordiyenko, G., & Pandey, R. (2014). Ionospheric response to the geomagnetic storm of 15 May 2005 over midlatitudes in the day and night sectors simultaneously. *Journal of Geophysical Research: Space Physics*, *119*, 5020–5031. <https://doi.org/10.1002/2013JA019679>

Heelis, R. A. (2017). Longitude and hemispheric dependencies in storm-enhanced density. In T. Fuller-Rowell, E. Yizengaw, P. H. Doherty, & S. Basu (Eds.), *Ionospheric space weather: Longitude and hemispheric dependences and lower atmosphere forcing*, *Geophysical Monograph*, *220* (pp. 61–70). Washington, DC: American Geophysical Union.

Heelis, R. A., & Coley, W. R. (2007). Variations in the low- and middle-latitude topside ion concentration observed by DMSP during superstorm events. *Journal of Geophysical Research*, *112*, A08310. <https://doi.org/10.1029/2007JA012326>

Heelis, R. A., Sojka, J. J., David, M., & Schunk, R. W. (2009). Storm time density enhancements in the middle-latitude dayside ionosphere. *Journal of Geophysical Research*, *114*, A03315. <https://doi.org/10.1029/2008JA013690>

Huang, C. S. (2008). Global characteristics of ionospheric electric fields and disturbances during the first hours of magnetic storms. *Advances in Space Research*, *41*, 527–538. <https://doi.org/10.1016/j.asr.2007.08.026>

Immel, T. J., & Mannucci, A. J. (2013). Ionospheric redistribution during geomagnetic storms. *Journal of Geophysical Research: Space Physics*, *118*, 7928–7939. <https://doi.org/10.1002/2013JA018919>

Iyemori, T. (1990). Storm-time magnetospheric currents inferred from mid-latitude geomagnetic field variations. *Journal of Geomagnetism and Geolectricity*, *42*(11), 1249–1265. <https://doi.org/10.5636/jgg.42.1249>

Iyemori, T., & Rao, D. R. K. (1996). Decay of the Dst field of geomagnetic disturbance after substorm onset and its implication to storm-substorm relation. *Annales de Geophysique*, *14*(6), 608–618. <https://doi.org/10.1007/s00585-996-0608-3>

Jakowski, N., Sardon, E., Engler, E., Jungstand, A., & Klahn, D. (1996). Relationships between GPS-signal propagation errors and EISCAT observations. *Annales de Geophysique*, *14*(12), 1429–1436. <https://www.ann-geophys.net/14/1429/1996/angeo-14-1429-1996>, <https://doi.org/10.1007/s00585-996-1429-0>

Kelley, M. C., Vlasov, M. N., Foster, J. C., & Coster, A. J. (2004). A quantitative explanation for the phenomenon known as storm-enhanced density. *Geophysical Research Letters*, *31*, L19809. <https://doi.org/10.1029/2004GL020875>

Kikuchi, T. (2014). Transmission line model for the near-instantaneous transmission of the ionospheric electric field and currents to the equator. *Journal of Geophysical Research: Space Physics*, *119*, 1131–1156. <https://doi.org/10.1002/2013JA019515>

Kikuchi, T., & Hashimoto, K. K. (2016). Transmission of the electric fields to the low latitude ionosphere in the magnetosphere-ionosphere current circuit. *Science Letters*, *41*(9), 927–936. [https://doi.org/10.1016/0021-9169\(79\)90094-1](https://doi.org/10.1016/0021-9169(79)90094-1)

Kikuchi, T., Hashimoto, K. K., Kitamura, T.-I., Tachihara, H., & Fejer, B. (2003). Equatorial counter-electrojets during substorms. *Journal of Geophysical Research*, *108*(A11), 1406. <https://doi.org/10.1029/2003JA009915>

- Kikuchi, T., Hashimoto, K. K., & Nozaki, K. (2008). Penetration of the electric fields to the equator during a geomagnetic storm. *Journal of Geophysical Research*, *113*, A06214. <https://doi.org/10.1029/2007JA012628>
- Kikuchi, T., Luhr, H., Kitamura, T., Saka, O., & Schlegel, K. (1996). Direct penetration of the polar electric field to the equator during a DP 2 event as detected by the auroral and equatorial magnetometer chains and the EISCAT radar. *Journal of Geophysical Research*, *101*(A8), 17,161–17,173. <https://doi.org/10.1029/96JA01299>
- Liu, J., Wang, W., Burns, A., Solomon, S. C., Zhang, S., Zhang, Y., & Huang, C. (2016). Relative importance of horizontal and vertical transports to the formation of ionospheric storm-enhanced density and polar tongue of ionization. *Journal of Geophysical Research: Space Physics*, *121*, 8121–8133. <https://doi.org/10.1002/2016JA022882>
- Liu, J., Wang, W., Burns, A., Yue, X., Zhang, S., Zhang, Y., & Huang, C. (2016). Profiles of ionospheric storm-enhanced density during the 17 March 2015 great storm. *Journal of Geophysical Research: Space Physics*, *121*, 727–744. <https://doi.org/10.1002/2015JA021832>
- Maruyama, T. (2006). Extreme enhancement in total electron content after sunset 8 November 2004 and its connection with storm enhanced density. *Geophysical Research Letters*, *33*, L20111. <https://doi.org/10.1029/2006GL027367>
- Maruyama, T., Ma, G., & Nakamura, M. (2004). Signature of TEC storm on 6 November 2001 derived from dense GPS receiver network and ionosonde chain over Japan. *Journal of Geophysical Research*, *109*, A10302. <https://doi.org/10.1029/2004JA010451>
- Maruyama, T., Ma, G., & Tsugawa, T. (2013). Storm-induced plasma stream in the low-latitude to midlatitude ionosphere. *Journal of Geophysical Research: Space Physics*, *118*(9), 5931–5941. <https://doi.org/10.1002/jgra.50541>
- Mendillo, M., Papagiannis, M. D., & Klobuchar, J. A. (1972). Average behavior of the midlatitude F-region parameters N_T , N_{max} and t during geomagnetic storms. *Journal of Geophysical Research*, *77*(25), 4891–4895. <https://doi.org/10.1029/JA077i025p04891>
- Moldwin, M. B., Zou, S., & Heine, T. (2016). The story of plumes: The development of a new conceptual framework for understanding magnetosphere and ionosphere coupling. *Annales de Geophysique*, *34*(12), 1243–1253. <https://doi.org/10.5194/angeo-34-1243-2016>
- Nakamizo, A., Hiraki, Y., Ebihara, Y., Kikuchi, T., Seki, K., Hori, T., et al. (2012). Effect of R2-FAC development on the ionospheric electric field pattern deduced by a global ionospheric potential solver. *Journal of Geophysical Research*, *117*, A09231. <https://doi.org/10.1029/2012JA017669>
- Nakamizo, A., & Yoshikawa, Y. (2019). Deformation of ionospheric potential pattern by ionospheric hall polarization. *Journal of Geophysical Research: Space Physics*, *124*, 7553–7580. <https://doi.org/10.1029/2018JA026013>
- Nishida, A. (1968). Coherence of geomagnetic DP 2 magnetic fluctuations with interplanetary magnetic variations. *Journal of Geophysical Research*, *73*(17), 5549–5559. <https://doi.org/10.1029/JA073i017p05549>
- Nishitani, N., Ruohoniemi, J. M., Lester, M., Baker, J. B. H., Koustov, A. V., Shepherd, S. G., et al. (2019). Review of the accomplishments of mid-latitude Super Dual Auroral Radar Network (SuperDARN) HF radars (2019). *Progress in Earth and Planetary Science*, *6*(27). <https://doi.org/10.1186/s40645-019-0270-5>
- Nose, M., Iyemori, T., Sugiura, M., & Kamei, T. (2015). *World Data Center for Geomagnetism, Kyoto Geomagnetic AE index*. <https://doi.org/10.17593/15031-54800>
- Otsuka, Y., Ogawa, T., Saito, A., Tsugawa, T., Fukao, S., & Miyazaki, S. (2002). A new technique for mapping of total electron content using GPS network in Japan. *Earth, Planets and Space*, *54*(1), 63–70. <https://doi.org/10.1186/BF03352422>
- Papagiannis, M. D., Mendillo, M., & Klobuchar, J. A. (1971). Simultaneous storm-time increases of the ionospheric total electron content and the geomagnetic field in the dusk sector. *Planetary and Space Science*, *19*(5), 503–511. [https://doi.org/10.1016/0032-0633\(71\)90166-8](https://doi.org/10.1016/0032-0633(71)90166-8)
- Piñón, D. A., Gómez, D. D., Smalley, R., Cimbaro, S. R., Lauría, E. A., & Bevis, M. G. (2018). The history, state, and future of the Argentine continuous satellite monitoring network and its contributions to geodesy in Latin America. *Seismological Research Letters*, *89*(2A), 475–482. <https://doi.org/10.1785/0220170162>
- Pröls, G. W. (1997). Magnetic storm associated perturbations of the upper atmosphere. In B. T. Tsurutani, W. D. Gonzales, Y. Kamide, & J. K. Arballo (Eds.), *Magnetic storms, Geophysical Monograph 98* (pp. 183–202). Washington, DC: American Geophysical Union.
- Rastogi, R. G., & Klobuchar, J. A. (1990). Ionospheric electron content within the equatorial F₂ layer anomaly belt. *Journal of Geophysical Research*, *95*(A11), 19,045–19,052. <https://doi.org/10.1029/JA095iA11p19045>
- Reinisch, B. W., & Galkin, I. A. (2011). Global Ionospheric Radio Observatory (GIRO). *Earth, Planets, Spaceflight*, *63*(4), 377–381. <https://doi.org/10.5047/eps.2011.03.001>
- Rishbeth, H., Heelis, R. A., Makela, J. J., & Basu, S. (2010). Storming the Bastille: The effect of electric fields on the ionospheric F-layer. *Annales de Geophysique*, *28*(4), 977–981. <https://doi.org/10.5194/angeo-28-977-2010>
- Shepherd, S. G. (2014). Altitude-adjusted corrected geomagnetic coordinates: Definition and functional approximations. *Journal of Geophysical Research: Space Physics*, *119*, 7501–7521. <https://doi.org/10.1002/2014JA020264>
- Shinbori, A., Otsuka, Y., Tsugawa, T., Nishioka, M., Kumamoto, A., Tsuchiya, F., et al. (2018). Temporal and spatial variations of storm time midlatitude ionospheric trough based on global GNSS-TEC and Arase satellite observations. *Geophysical Research Letters*, *45*, 7362–7370. <https://doi.org/10.1029/2018GL078723>
- Sori, T., Shinbori, A., Otsuka, Y., Tsugawa, T., & Nishioka, M. (2019). Characteristics of GNSS total electron content enhancements over the midlatitudes during a geomagnetic storm on 7 and 8 November 2004. *Journal of Geophysical Research: Space Physics*, *124*(12), 10,376–10,394. <https://doi.org/10.1029/2019JA026713>
- Tanaka, T. (1995). Generation mechanisms for magnetosphere-ionosphere current systems deduced from a three-dimensional MHD simulation of the solar wind-magnetosphere-ionosphere coupling processes. *Journal of Geophysical Research*, *100*(A7), 12,057–12,074. <https://doi.org/10.1029/95JA00419>
- Tanaka, T., Watanabe, M., Den, M., Fujita, S., Ebihara, Y., Kikuchi, T., et al. (2016). Generation of field-aligned current (FAC) and convection through the formation of pressure regimes: Correction for the concept of Dungey's convection. *Journal of Geophysical Research: Space Physics*, *121*, 8695–8711. <https://doi.org/10.1002/2016JA022822>
- Tanaka, Y., Shinbori, A., Hori, T., Koyama, Y., Abe, S., Umemura, N., et al. (2013). Analysis software for upper atmospheric data developed by the IUGONET project and its application to polar science. *Advances in Polar Science*, *24*(4), 231–240. <https://doi.org/10.3724/SP.J.1085.2013.00231>
- Thomas, E. G., Baker, J. B. H., Ruohoniemi, J. M., Clausen, L. B. N., Coster, A. J., Foster, J. C., & Erickson, P. J. (2013). Direct observations of the role of convection electric field in the formation of a polar tongue of ionization from storm enhanced density. *Journal of Geophysical Research: Space Physics*, *118*, 1180–1189. <https://doi.org/10.1002/jgra.50116>
- Tsugawa, T., Kotake, N., Otsuka, Y., & Saito, A. (2007). Medium-scale traveling ionospheric disturbances observed by GPS receiver network in Japan: A short review. *GPS Solutions*, *11*(2), 139–144. <https://doi.org/10.1007/s10291-006-0045-5>
- Tsugawa, T., Nishioka, M., Ishii, M., Hozumi, K., Saito, S., Shinbori, A., et al. (2018). Total electron content observations by dense regional and worldwide international networks of GNSS. *Journal of Disaster Research*, *13*(3), 535–545. <https://doi.org/10.20965/jdr.2018.p0535>

- Tsuji, Y., Shinbori, A., Kikuchi, T., & Nagatsuma, T. (2012). Magnetic latitude and local time distributions of ionospheric currents during a geomagnetic storm. *Journal of Geophysical Research*, *117*, A07318. <https://doi.org/10.1029/2012JA017566>
- Tsurutani, B., Mannucci, A., Iijima, B., Abdu, M. A., Sobral, J. H. A., Gonzalez, W., et al. (2004). Global dayside ionospheric uplift and enhancement associated with interplanetary electric fields. *Journal of Geophysical Research*, *109*, A08302. <https://doi.org/10.1029/2003JA010342>
- Yang, N., Le, H., & Liu, L. (2015). Statistical analysis of ionospheric mid-latitude trough over the northern hemisphere derived from GPS total electron content data. *Earth, Planets and Space*, *67*(1), 196. <https://doi.org/10.1186/s40623-015-0365-1>
- Yang, N., Le, H., & Liu, L. (2016). Statistical analysis of the mid-latitude trough position during different categories of magnetic storms and different storm intensities. *Earth, Planets and Space*, *68*(1), 171. <https://doi.org/10.1186/s40623-016-0554-6>
- Yizengaw, E., Moldwin, M. B., & Galvan, D. A. (2006). Ionospheric signatures of a plasmaspheric plume over Europe. *Geophysical Research Letters*, *33*, L17103. <https://doi.org/10.1029/2006GL026597>
- Zhao, B., Wan, W., & Liu, L. (2005). Responses of equatorial anomaly to the October–November 2003 superstorms. *Annales de Geophysique*, *23*(3), 693–706. <https://doi.org/10.5194/angeo-23-693-2005>
- Zou, S., Moldwin, M. B., Ridley, A. J., Nicolls, M. J., Coster, A. J., Thomas, E. G., & Ruohoniemi, J. M. (2014). On the generation/decay of the storm-enhanced density plumes: Role of the convection flow and field-aligned ion flow: Generation and decay of SED plumes. *Journal of Geophysical Research: Space Physics*, *119*(10), 8543–8559. <https://doi.org/10.1002/2014JA020408>
- Zou, S., Ridley, A. J., Moldwin, M. B., Nicolls, M. J., Coster, A. J., Thomas, E. G., & Ruohoniemi, J. M. (2013). Multi-instrument observations of SED during 24–25 October 2011 storm: Implications for SED formation processes. *Journal of Geophysical Research: Space Physics*, *118*, 7798–7809. <https://doi.org/10.1002/2013JA018860>